

DeepPoseKit, a software toolkit for fast and robust animal pose estimation using deep learning

Jacob M. Graving^{1,2,3,*}, Daniel Chae⁴, Hemal Naik^{1,2,3,5}, Liang Li^{1,2,3}, Benjamin Koger^{1,2,3}, Blair R. Costelloe^{1,2,3}, Iain D. Couzin^{1,2,3,*}

*For correspondence:

jgraving@gmail.com; icouzin@ab.mpg.de

¹Department of Collective Behaviour, Max Planck Institute of Animal Behavior, 78464 Konstanz, Germany; ²Department of Biology, University of Konstanz, 78464 Konstanz, Germany; ³Centre for the Advanced Study of Collective Behaviour, University of Konstanz, 78464 Konstanz, Germany; ⁴Department of Computer Science, Princeton University, 08544 Princeton, NJ, USA; ⁵Chair for Computer Aided Medical Procedures, Technische Universität München, 80333 Munich, Germany

Abstract Quantitative behavioral measurements are important for answering questions across scientific disciplines—from neuroscience to ecology. State-of-the-art deep-learning methods offer major advances in data quality and detail by allowing researchers to automatically estimate locations of an animal's body parts directly from images or videos. However, currently-available animal pose estimation methods have limitations in speed and robustness. Here we introduce a new easy-to-use software toolkit, *DeepPoseKit*, that addresses these problems using an efficient multi-scale deep-learning model, called *Stacked DenseNet*, and a fast GPU-based peak-detection algorithm for estimating keypoint locations with subpixel precision. These advances improve processing speed >2x with no loss in accuracy compared to currently-available methods. We demonstrate the versatility of our methods with multiple challenging animal pose estimation tasks in laboratory and field settings—including groups of interacting individuals. Our work reduces barriers to using advanced tools for measuring behavior and has broad applicability across the behavioral sciences.

Introduction

Understanding the relationships between individual behavior, brain activity (reviewed by *Krakauer et al. 2017*), and collective and social behaviors (*Rosenthal et al., 2015; Strandburg-Peshkin et al., 2013; Jolles et al., 2017; Klibaite et al., 2017; Klibaite and Shaevitz, 2019*) is a central goal of the behavioral sciences—a field that spans disciplines from neuroscience to psychology, ecology, and genetics. Measuring and modelling behavior is key to understanding these multiple scales of complexity, and, with this goal in mind, researchers in the behavioral sciences have begun to integrate theory and methods from physics, computer science, and mathematics (*Anderson and Perona, 2014; Berman, 2018; Brown and De Bivort, 2018*). A cornerstone of this interdisciplinary revolution is the use of state-of-the-art computational tools, such as computer vision algorithms, to automatically measure locomotion and body posture (*Dell et al., 2014*). Such a rich description of animal movement then allows for modeling, from first principles, the full behavioral repertoire of animals (*Stephens et al., 2011; Berman et al., 2014a, 2016; Wiltchko et al., 2015; Johnson et al., 2016b; Todd et al., 2017; Klibaite et al., 2017; Markowitz et al., 2018; Klibaite and Shaevitz, 2019; Costa et al., 2019*). Tools for automatically measuring animal movement represent a vital first step toward developing unified theories of behavior across scales (*Berman, 2018; Brown and De Bivort, 2018*). Therefore, technical factors like scalability, robustness, and usability are issues of critical importance, especially as researchers across disciplines begin to increasingly rely on these methods.

Two of the latest contributions to the growing toolbox for quantitative behavioral analysis are from *Mathis et al. (2018)* and *Pereira et al. (2019)*, who make use of a popular type of machine learning model called *convolutional neural networks*, or *CNNs* (*LeCun et al. 2015; Appendix 2*), to automatically measure detailed representations of animal posture—structural *keypoints*, or *joints*, on the animal's body—directly from images

and without markers. While these methods offer a major advance over conventional methods with regard to data quality and detail, they have disadvantages in terms of speed and robustness, which may limit their practical applications. To address these problems, we introduce a new software toolkit, called *DeepPoseKit*, with methods that are fast, robust, and easy-to-use. We run experiments using multiple datasets to compare our new methods with those from *Mathis et al. (2018)* and *Pereira et al. (2019)*, and we find that our approach offers considerable improvements. These results also demonstrate the flexibility of our toolkit for both laboratory and field situations and exemplify the wide applicability of our methods across a range of species and experimental conditions.

Measuring animal movement with computer vision

Collecting high-quality behavioral data is a challenging task, and while direct observations are important for gathering qualitative data about a study system, a variety of automated methods for quantifying movement have become popular in recent years (*Dell et al., 2014; Anderson and Perona, 2014; Kays et al., 2015*). Methods like video monitoring and recording help to accelerate data collection and reduce the effects of human intervention, but the task of manually scoring videos is time consuming and suffers from the same limitations as direct observation, namely observer bias and mental fatigue. Additionally, due to limitations of human observers' ability to process information, many studies that rely on manual scoring use relatively small datasets to estimate experimental effects, which can lead to increased rates of statistical errors. Studies that lack the statistical resolution to robustly test hypotheses (commonly called "power" in frequentist statistics) also raise concerns about the use of animals for research, as statistical errors caused by sparse data can impact researchers' ability to accurately answer scientific questions. These limitations have led to the development of automated methods for quantifying behavior using advanced imaging technologies (*Dell et al., 2014*) as well as sophisticated tags and collars with GPS, accelerometry, and acoustic-recording capabilities (*Kays et al., 2015*). Tools for automatically measuring the behavior of individuals now play a central role in our ability to study the neurobiology and ecology of animals, and reliance on these technologies for studying animal behavior will only increase in the future.

The rapid development of computer vision hardware and software in recent years has allowed for the use of automated image-based methods for measuring behavior across many experimental contexts (*Dell et al., 2014*). Early methods for quantifying movement with these techniques required highly-controlled laboratory conditions. However, because animals exhibit different behaviors depending on their surroundings (*Strandburg-Peshkin et al., 2017; Francisco et al., 2019; Akhund-Zade et al., 2019*), laboratory environments are often less than ideal for studying many natural behaviors. Most conventional computer vision methods are also limited in their ability to accurately track groups of individuals over time, but nearly all animals are social at some point in their life and exhibit specialized behaviors when in the presence of conspecifics (*Strandburg-Peshkin et al., 2013; Rosenthal et al., 2015; Jolles et al., 2017; Klibaite et al., 2017; Klibaite and Shaevitz, 2019; Francisco et al., 2019; Versace et al., 2019*). These methods also commonly track only the animal's center of mass, which reduces the behavioral output of an individual to a two-dimensional or three-dimensional particle-like trajectory. While trajectory data are useful for many experimental designs, the behavioral repertoire of an animal cannot be fully described by its aggregate locomotory output. For example, stationary behaviors, like grooming and antennae movements, or subtle differences in walking gaits cannot be reliably detected by simply tracking an animal's center of mass (*Berman et al., 2014a; Wiltchko et al., 2015*).

Together these factors have driven the development of software that can accurately track the positions of marked (*Crall et al., 2015; Graving, 2017; Wild et al., 2018; Boenisch et al., 2018*) or unmarked (*Pérez-Escudero et al., 2014; Romero-Ferrero et al., 2019*) individuals as well as methods that can quantify detailed descriptions of an animal's posture over time (*Stephens et al., 2011; Berman et al., 2014a; Wiltchko et al., 2015; Mathis et al., 2018; Pereira et al., 2019*). Recently these advancements have been further improved through the use of deep learning, a class of machine learning algorithms that learn complex statistical relationships from data (*LeCun et al., 2015*). Deep learning has opened the door to accurately tracking large groups of marked (*Wild et al., 2018; Boenisch et al., 2018*) or unmarked (*Romero-Ferrero et al., 2019*) individuals and has made it possible to measure the body posture of animals in nearly any context—including in the wild (*Nath et al., 2019*)—by tracking the positions of user-defined body parts (*Mathis et al., 2018; Pereira et al., 2019*). These advances have drastically increased the quality and quantity, as well as the diversity, of behavioral data that are potentially available to researchers for answering scientific questions.

Animal pose estimation using deep learning

In the past, conventional methods for measuring posture with computer vision relied on species-specific algorithms (*Uhlmann et al., 2017*), highly-specialized or restrictive experimental setups (*Mendes et al., 2013; Kain et al., 2013*), attaching intrusive physical markers to the study animal (*Kain et al., 2013*), or some combination

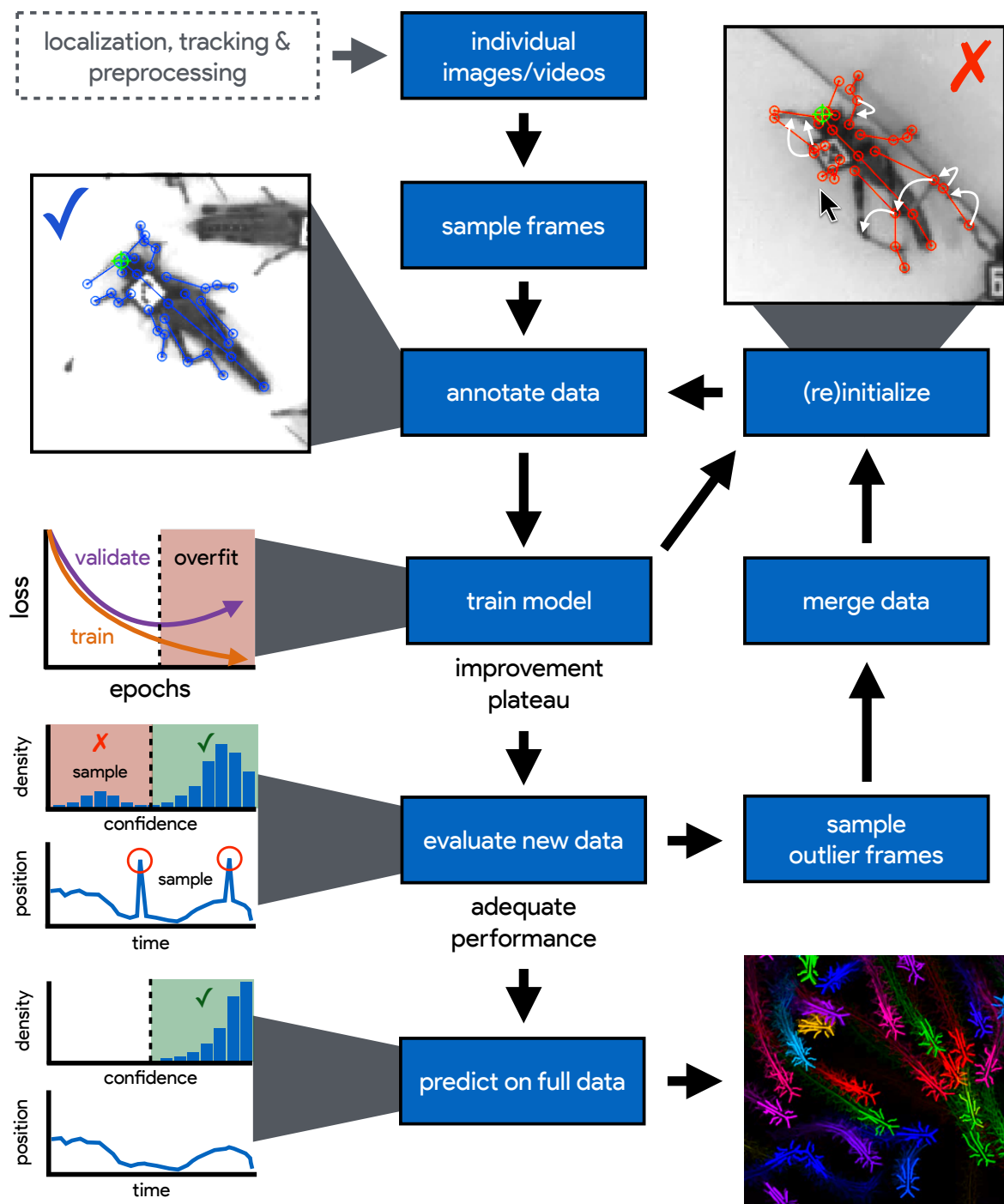


Figure 1. An illustration of the workflow for DeepPoseKit. Multi-individual images are localized, tracked, and preprocessed into individual images, which is not required for single-individual image datasets. An initial image set is sampled, annotated, and then iteratively updated using the active learning approach described by *Pereira et al. (2019)* (see Appendix 3). As annotations are made, the model is trained (Figure 2) with the current training set and keypoint locations are initialized for unannotated data to reduce the difficulty of further annotations. This is repeated until there is a noticeable improvement plateau for the initialized data—where the annotator is providing only minor corrections—and for the validation error when training the model (Appendix 1 Figure 4). New data from the full dataset are evaluated with the model, and the training set is merged with new examples that are sampled based on the model's predictive performance, which can be assessed with techniques described by *Mathis et al. (2018)*; *Nath et al. (2019)* for identifying outlier frames and minimizing extreme prediction errors—shown here as the distribution of confidence scores predicted by the model and predicted body part positions with large temporal derivatives—indicating extreme errors. This process is repeated as necessary until performance is adequate when evaluating new data. The pose estimation model can then be used to make predictions for the full data set, and the data can be used for further analysis.

Figure 1–video 1. A visualization of the posture data output for a group of locusts (5x speed) <https://youtu.be/hCa2zaoUWfs>.

thereof. These methods also typically required expert computer-vision knowledge to use, were limited in the number or type of body parts that could be tracked (*Mendes et al., 2013*), involved capturing and handling the study animals to attach markers (*Kain et al., 2013*)—which is not possible for many species—and despite best efforts to minimize human involvement, often required manual intervention to correct errors (*Uhlmann et al., 2017*). All of these methods were built to work for a small range of conditions and typically required considerable effort to adapt to novel contexts.

In contrast to conventional computer-vision methods, modern deep-learning-based methods can be used to achieve near human-level accuracy in almost any scenario by manually annotating data (Figure 1)—known as a *training set*—and training a general-purpose image-processing algorithm—a convolutional neural network or CNN—to automatically estimate the locations of an animal's body parts directly from images (Figure 2). State-of-the-art machine learning methods, like CNNs, use these training data to parameterize a model describing the statistical relationships between a set of input data—i.e., images—and the desired output distribution—i.e., posture keypoints. After adequate training, a model can be used to make predictions on previously-unseen data from the same dataset—inputs that were not part of the training set, which is known as *inference*. In other words, these models are able to generalize human-level expertise at scale after having been trained on only a relatively small number of examples. We provide more detailed background information on using CNNs for pose estimation in Appendices 2–6.

Similar to conventional pose estimation methods, the task of implementing deep-learning models in software and training them on new data is complex and requires expert knowledge. However, in most cases, once the underlying model and training routine are implemented, a high-accuracy pose estimation model for a novel context can be built with minimal modification—often just by changing the training data. With a simplified toolkit and high-level software interface designed by an expert, even scientists with limited computer-vision knowledge can begin to apply these methods to their research. Once the barriers for implementing and training a model are sufficiently reduced, the main bottleneck for using these methods becomes collecting an adequate training set—a labor-intensive task made less time-consuming by techniques described in Appendix 3.

Mathis et al. (2018) and *Pereira et al. (2019)* were the first to popularize the use of CNNs for animal pose estimation. These researchers built on work from the human pose estimation literature (e.g., *Andriluka et al. 2014; Insafutdinov et al. 2016; Newell et al. 2016*) using a type of *fully-convolutional neural network* or *F-CNN* (*Long et al. 2015*; Appendix 4) often referred to as an *encoder-decoder* model (Appendix 4 Box 1). These models are used to measure animal posture by training the network to transform images into probabilistic estimates of keypoint locations, known as *confidence maps* (shown in Figure 2), that describe the body posture for one or more individuals. These confidence maps are processed to produce the 2-D spatial coordinates of each keypoint, which can then be used for further analysis.

While deep-learning models typically need large amounts of training data, both *Mathis et al. (2018)* and *Pereira et al. (2019)* have demonstrated that near human-level accuracy can be achieved with few training examples (Appendix 3). In order to ensure generalization to large datasets, both groups of researchers introduced ideas related to iteratively refining the training set used for model fitting (*Mathis et al., 2018; Pereira et al., 2019*). In particular, *Pereira et al. (2019)* describe a technique known as *active learning* where a trained model is used to initialize new training data and reduce annotation time (Appendix 3). *Mathis et al. (2018)* describe multiple techniques that can be used to further refine training data and minimize errors when making predictions on the full dataset. Simple methods to accomplish this include filtering data or selecting new training examples based on confidence scores or the entropy of the confidence maps from the model output. *Nath et al. (2019)* also introduced the use temporal derivatives (i.e., speed and acceleration) and autoregressive models to identify outlier frames, which can then be labeled to refine the training set or excluded from further analysis on the final dataset (Figure 1).

Pose estimation models and the speed-accuracy trade-off

Mathis et al. (2018) developed their pose estimation model, which they call *DeepLabCut*, by modifying a previously-published model called *DeeperCut* (*Insafutdinov et al., 2016*). The *DeepLabCut* model (*Mathis et al., 2018*), like the *DeeperCut* model, is built on the popular *ResNet* architecture (*He et al., 2016*)—a state-of-the-art deep-learning model used for image classification. This choice is advantageous because the use of a popular architecture allows for incorporating a pre-trained encoder to improve performance and reduce the number of required training examples (*Mathis et al., 2018*), known as *transfer learning* (*Pratt 1993*; Appendix 3)—although, as will be seen, transfer learning appears to offer little improvement over a randomly-initialized model. However, this choice of a pre-trained architecture is also disadvantageous as the model is *overparameterized* with >25 million parameters. Overparameterization allows the model to make accurate predictions, but this may come with the cost of slow inference. To alleviate these effects, work from *Mathis and Warren (2018)* showed that inference speed for the *DeepLabCut* model (*Mathis et al., 2018*) can be improved by decreasing the resolution

of input images, but this is achieved at the expense of accuracy.

With regard to model design, *Pereira et al. (2019)* implement a modified version of a model called *SegNet* (*Badrinarayanan et al., 2015*), which they call *LEAP* (LEAP Estimates Animal Pose), that attempts to limit model complexity and overparameterization with the goal of maximizing inference speed (see Appendix 6)—however, our comparisons from this paper suggest *Pereira et al. (2019)* achieved only limited success compared to the DeepLabCut model (*Mathis et al., 2018*). The LEAP model is advantageous because it is explicitly designed for fast inference but has disadvantages such as a lack of robustness to data variance, like rotations or shifts in lighting, and an inability to generalize to new experimental setups. Additionally, to achieve maximum performance, the training routine for the LEAP model introduced by *Pereira et al. (2019)* requires computationally expensive preprocessing that is not practical for many datasets, which makes it unsuitable for a wide range of experiments (see Appendix 6 for more details).

Together the methods from *Mathis et al. (2018)* and *Pereira et al. (2019)* represent the two extremes of a phenomenon known as the *speed-accuracy trade-off* (*Huang et al., 2017b*)—an active area of research in the machine learning literature. *Mathis et al. (2018)* prioritize accuracy over speed by using a large overparameterized model (*Insafutdinov et al., 2016*), and *Pereira et al. (2019)* prioritize speed over accuracy by using a smaller less-robust model. While this speed-accuracy trade-off can limit the capabilities of CNNs, there has been extensive work to make these models more efficient without impacting accuracy (e.g., *Chollet 2017; Huang et al. 2017a; Sandler et al. 2018*). To address the limitations of this trade-off, we apply recent developments from the machine learning literature and provide an effective solution to the problem.

In the case of F-CNN models used for pose estimation, improvements in efficiency and robustness have been made through the use of *multi-scale inference* (Appendix 4 Box 1) by increasing connectivity between the model's many layers across multiple spatial scales (Appendix 4 Figure 1). Multi-scale inference implicitly allows the model to simultaneously integrate large-scale global information, such as the lighting, image background, or the orientation of the focal individual's body trunk; information from intermediate scales like anatomical geometry related to cephalization and bilateral symmetry; and fine-scale local information that could include differences in color, texture, or skin patterning for specific body parts. This multi-scale design gives the model capacity to learn the hierarchical relationships between different spatial scales and efficiently aggregate them into a joint representation when solving the posture estimation task (see Box 1 and Appendix 4 Figure 1 for further discussion)

Individual vs. multiple pose estimation

Most work on human pose estimation now focuses on estimating the pose of multiple individuals in an image (e.g., *Cao et al. 2017*). For animal pose estimation, the methods from *Pereira et al. (2019)* are limited to estimating posture for single individuals—known as *individual pose estimation*—while the methods from *Mathis et al. (2018)* can also be extended to estimate posture for multiple individuals simultaneously—known as *multiple pose estimation*. However, the majority of work on multiple pose estimation, including *Mathis et al. (2018)*, has not adequately solved the tracking problem of linking individual posture data across frames in a video, especially after visual occlusions, which are common in many behavioral experiments—although recent work has attempted to address this problem (*Iqbal et al., 2017; Andriluka et al., 2018*). Additionally, as the name suggests, the task of multiple pose estimation requires exhaustively annotating images of multiple individuals—where every individual in the image must be annotated to prevent the model from learning conflicting information. This type of annotation task is even more laborious and time consuming than annotations for individual pose estimation and the amount of labor increases proportionally with the number of individuals in each frame, which makes this approach intractable for many experimental systems.

Reliably tracking the position of individuals over time is important for most behavioral studies, and there are a number of diverse methods already available for solving this problem (*Pérez-Escudero et al., 2014; Crall et al., 2015; Graving, 2017; Romero-Ferrero et al., 2019; Wild et al., 2018; Boenisch et al., 2018*). Therefore, to avoid solving an already-solved problem of tracking individuals and to circumvent the cognitively complex task of annotating data for multiple pose estimation, the work we describe in this paper is purposefully limited to individual pose estimation—where each image contains only a single focal individual, which may be cropped from a larger multi-individual image after localization and tracking. We introduce a top-down posture estimation framework that can be readily adapted to existing behavioral analysis workflows, which could include any method for localizing and tracking individuals.

The additional step of localizing and tracking individuals naturally increases the processing time for producing posture data from raw image data, which varies depending on the algorithms being used and the number of individuals in each frame. While tracking and localization may not be practical for all experimental systems, which could make our methods difficult to apply "out-of-the-box", the increased processing time from automated tracking algorithms is a reasonable trade-off for most systems given the costly alternative of increased manual

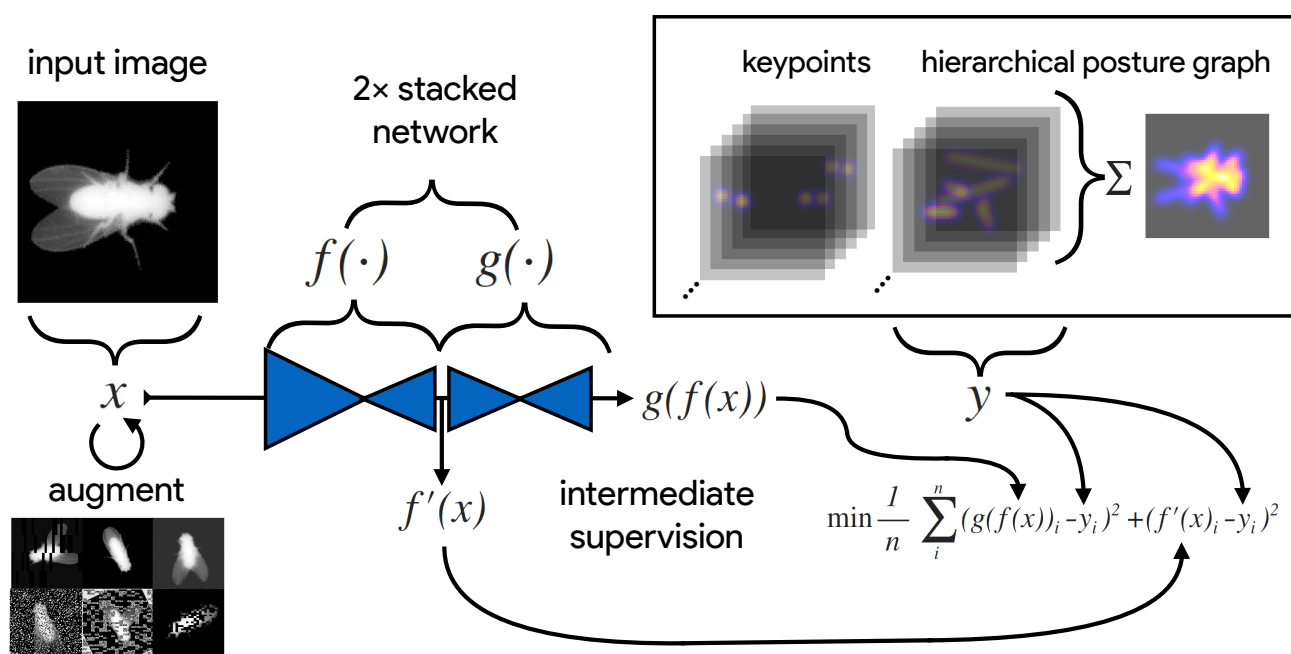


Figure 2. An illustration of the model training process for our Stacked DenseNet model in DeepPoseKit (see Appendix 2 for details about training models). Input images x (**top-left**) are augmented (**bottom-left**) with various spatial transformations (rotation, translation, scale, etc.) followed by noise transformations (dropout, additive noise, blurring, contrast, etc.) to improve the robustness and generalization of the model. The ground truth annotations are then transformed with matching spatial augmentations (not shown for the sake of clarity) and used to draw the confidence maps y for the keypoints and hierarchical posture graph (**top-right**). The images x are then passed through the network to produce a multidimensional array $g(f(x))$ —a stack of images corresponding to the keypoint and posture graph confidence maps for the ground truth y . Mean squared error between the outputs for both networks $g(f(x))$ and $f'(x)$ and the ground truth data y is then minimized (**bottom-right**), where $f'(x)$ indicates a subset of the output from $f(x)$ —only those feature maps being optimized to reproduce the confidence maps for the purpose of intermediate supervision (Appendix 5). The loss function is minimized until the validation loss stops improving—indicating that the model has converged or is starting to overfit to the training data.

labor when annotating data. This trade-off seems especially practical when considering that the posture data produced by most multiple pose estimation algorithms still need to be linked across video frames to maintain the identity of each individual, which is effectively a bottom-up method for achieving the same result. Limiting our methods to individual pose estimation also simplifies the pose detection problem as processing confidence maps produced by the model does not require computationally-expensive local peak detection and complex methods for grouping keypoints into individual posture graphs (e.g., *Insafutdinov et al. 2016*; *Cao et al. 2017*; Appendix 4). Additionally, because individual pose estimation is such a well-studied problem in computer vision, we can readily build on state-of-the-art methods for this task (see Appendices 4 and 5 for details).

Results

Here we introduce fast, flexible, and robust pose estimation methods, with a software interface—a high-level programming interface (API) and graphical user-interface (GUI) for annotations—that emphasizes usability. Our methods build on the state-of-the-art for individual pose estimation (*Newell et al. 2016*; Appendix 5), convolutional regression models (*Jégou et al. 2017*; Appendix 4 Box 1), and conventional computer vision algorithms (*Guizar-Sicairos et al., 2008*) to improve model efficiency and achieve faster, more accurate results on multiple challenging pose estimation tasks. We developed two model implementations—including a new model architecture that we call *Stacked DenseNet*—and a new method for processing confidence maps called *subpixel maxima* that provides fast and accurate peak detection for estimating keypoint locations with subpixel precision—even at low spatial resolutions. We also discuss a modification to incorporate a hierarchical posture graph for learning the multi-scale geometry between keypoints on the animal's body, which increases accuracy when training pose estimation models. We ran experiments to optimize our approach and compared our new models to the models from *Mathis et al. (2018)* (DeepLabCut) and *Pereira et al. (2019)* (LEAP) in terms of speed, accuracy, training time, and generalization ability. We benchmarked these models using three image datasets recorded in the laboratory and the field—including multiple interacting individuals that were first localized and cropped from larger, multi-individual images (see "Methods" for details).

240 An end-to-end pose estimation framework

241 We provide a full-featured, extensible, and easy-to-use software package that is written entirely in the Python
242 programming language (Python Software Foundation) and is built on the popular Keras deep-learning package
243 (Chollet et al., 2015)—using TensorFlow as a backend (Abadi et al., 2015). Our software is a complete, end-to-
244 end pipeline (Figure 1) with a custom GUI for creating annotated training data with active learning similar to
245 Pereira et al. (2019; Appendix 3), as well as a flexible pipeline for data augmentation (Jung 2018; Appendix 3;
246 shown in Figure 2), model training and evaluation (Figure 2; Appendix 2), and running inference on new data.
247 We designed our high-level programming interface using the same guidelines from Keras (Chollet et al., 2015)
248 to allow the user to go from idea to result as quickly as possible, and we organized our software into a Python
249 module called *DeepPoseKit*. The code, documentation, and examples for our entire software package are freely
250 available at <https://github.com/jgraving/deepposekit> under a permissive open-source license.

251 Our pose estimation models

252 To achieve the goal of “fast animal pose estimation” introduced by Pereira et al. (2019), while maintaining
253 the robust predictive power of models like DeepLabCut (Mathis et al., 2018), we implemented two fast pose
254 estimation models that extend the state-of-the-art model for individual pose estimation introduced by Newell
255 et al. (2016) and the current state-of-the-art for convolutional regression from Jégou et al. (2017). Our model
256 implementations use fewer parameters than both the DeepLabCut model (Mathis et al., 2018) and LEAP model
257 (Pereira et al., 2019) while simultaneously removing many of the limitations of these architectures.

258 In order to limit overparameterization while minimizing performance loss, we designed our models to allow
259 for multi-scale inference (Appendix 4 Box 1) while optimizing our model hyperparameters for efficiency. Our
260 first model is a novel implementation of *FC-DenseNet* from Jégou et al. (2017; Appendix 4 Box 1) arranged in a
261 stacked configuration similar to Newell et al. (2016; Appendix 5). We call this new model Stacked DenseNet, and
262 to the best of our knowledge, this is the first implementation of this model architecture in the literature—for
263 pose estimation or otherwise. Further details for this model are available in Appendix 8. Our second model
264 is a modified version of the *Stacked Hourglass* model from Newell et al. (2016; Appendix 5) with hyperparam-
265 eters that allow for changing the number of filters in each convolutional block to constrain the number of
266 parameters—rather than using 256 filters for all layers as described in Newell et al. (2016).

267 Subpixel keypoint prediction on the GPU allows for fast and accurate inference

268 In addition to implementing our efficient pose estimation models, we developed a new method to process model
269 outputs to allow for faster, more accurate predictions. When using a fully-convolutional posture estimation
270 model, the confidence maps produced by the model must be converted into coordinate values for the predictions
271 to be useful, and there are typically two choices for making this conversion. The first is to move the confidence
272 maps out of GPU memory and post-process them on the CPU. This solution allows for easy, flexible, and accurate
273 calculation of the coordinates with subpixel precision (Insafutdinov et al., 2016; Mathis et al., 2018). However,
274 CPU processing is not ideal because moving large arrays of data between the GPU and CPU can be costly, and
275 computation on the CPU is generally slower. The other option is to directly process the confidence maps on the
276 GPU and then move the coordinate values from the GPU to the CPU. This approach usually means converting
277 confidence maps to integer coordinates based on the row and column index of the global maximum for each
278 confidence map (Pereira et al., 2019). However, this means that, to achieve a precise estimation, the confidence
279 maps should be predicted at the full resolution of the input image, or larger, which slows down inference speed.

280 As an alternative to these two strategies, we introduce a new GPU-based convolutional layer that we call
281 *subpixel maxima*. This layer uses the fast, efficient, image registration algorithm introduced by Guizar-Sicairos
282 et al. (2008) to translationally align a centered two-dimensional Gaussian filter to each confidence map via
283 Fourier-based convolution. The translational shift between the filter and each confidence map allows us to
284 calculate the coordinates of the global maxima with high speed and subpixel precision. This technique allows
285 for accurate predictions of keypoint locations even if the model's confidence maps are dramatically smaller than
286 the resolution of the input image. We compared the accuracy of our subpixel maxima layer to an integer-based
287 maxima layer using the fly dataset from Pereira et al. (2019) (see “Methods”). We found significant accuracy
288 improvements across every downsampling configuration (Appendix 1 Figure 1a). Even with confidence maps at
289 $\frac{1}{8} \times$ the resolution of the original image, error did not drastically increase compared to full-resolution predictions.
290 Making predictions for confidence maps at such a downsampled resolution allows us to achieve very fast
291 inference >1000 Hz while maintaining high accuracy (Appendix 1 Figure 1b).

292 We also provide speed comparisons with the other models we tested and find that our Stacked DenseNet
293 model with our subpixel peak detection algorithm is faster than the DeepLabCut model (Mathis et al., 2018) for
294 both offline (batch size = 100) and real-time speeds (batch size = 1). While we find that our Stacked DenseNet
295 model is faster than the LEAP model (Pereira et al., 2019) for offline processing (batch size = 100), the LEAP

model (Pereira et al., 2019) is significantly faster for real-time processing (batch size = 1). Our Stacked Hourglass model (Newell et al., 2016) is about the same or slightly faster than Stacked DenseNet for offline speeds (batch size = 100), but is much slower for real-time processing (batch size = 1). Achieving fast pose estimation using CNNs typically relies on massively parallel processing on the GPU with large batches of data or requires downsampling the images to increase speed, which increases error (Mathis and Warren, 2018). These factors make fast and accurate real-time inference challenging to accomplish. Our Stacked DenseNet model, with a batch size of one, can run inference at ~30-110Hz—depending on the resolution of the predicted confidence maps (Appendix 1 Figure 1b). These speeds are faster than the DeepLabCut model (Mathis et al., 2018) and could be further improved by downsampling the input image resolution or reconfiguring the model with fewer parameters. This allows our methods to be flexibly used for real-time or closed-loop behavioral experiments with prediction errors similar to current state-of-the-art methods.

Learning multi-scale geometry between keypoints improves accuracy and reduces extreme errors

Minimizing extreme prediction errors is important to prevent downstream effects on any further behavioral analysis (Seethapathi et al., 2019)—especially in the case of analyses based on time-frequency transforms like those from Berman et al. (2014a, 2016); Klibaite et al. (2017); Todd et al. (2017); Klibaite and Shaevitz (2019) and Pereira et al. (2019) where high magnitude errors can cause inaccurate behavioral classifications. While effects of these extreme errors can be minimized using post-hoc filters and smoothing, these post-processing techniques can remove relevant high-frequency information from time-series data, so this solution is less than ideal. One way to minimize extreme errors when estimating posture is to incorporate multiple spatial scales when making predictions (e.g., Chen et al. 2017). Our pose estimation models are implicitly capable of using information from multiple scales (see Appendix 4 Box 1), but there is no explicit signal that optimizes the model to take advantage of this information when making predictions.

To remedy this, we modified the model's output to predict, in addition to keypoint locations, a hierarchical graph of edges describing the multi-scale geometry between keypoints—similar to the part affinity fields described by Cao et al. (2017). This was achieved by adding an extra set of confidence maps to the output where edges in the postural graph are represented by Gaussian-blurred lines the same width as the Gaussian peaks in the keypoint confidence maps. Our posture graph output then consists of four levels: (1) a set of confidence maps for the smallest limb segments in the graph (e.g., foot to ankle, knee to hip, etc.; Figure 2), (2) a set of confidence maps for individual limbs (e.g., left leg, right arm, etc.; Figure 3), (3) a map with the entire postural graph, and (4) a fully-integrated map that incorporates the entire posture graph and confidence peaks for all of the joint locations (Figure 2). Each level of the hierarchical graph is built from lower levels in the output, which forces the model to learn correlated features across multiple scales when making predictions.

We find that training our Stacked DenseNet model to predict a hierarchical posture graph reduces keypoint prediction error (Appendix 1 Figure 2), and because the feature maps for the posture graph can be removed from the final output during inference, this effectively improves prediction accuracy for free. Both the mean and variance of the error distributions were lower when predicting the posture graph, which suggests that learning multi-scale geometry both decreases error on average and helps to reduce extreme prediction errors. The overall effect size for this decrease in error is fairly small (<1 pixel average reduction in error), but based on the results from the zebra dataset, this modification more dramatically improves performance for datasets with higher-variance images and sparse posture graphs. Predicting the posture graph may be especially useful for animals with long slender appendages such as insect legs and antennae where prediction errors are likely to occur due to occlusions and natural variation in the movement of these body parts. These results also suggest that annotating multiple keypoints to incorporate an explicit signal for multi-scale information may help improve prediction accuracy for a specific body part of interest.

Stacked DenseNet is fast and robust

We benchmarked our new model implementations against the models (Pereira et al., 2019) and Mathis et al. (2018). We find that our Stacked DenseNet model outperforms both the LEAP model (Pereira et al., 2019) and the DeepLabCut model (Mathis et al., 2018) in terms of speed while also achieving much higher accuracy than the LEAP model (Pereira et al., 2019) with similar accuracy to the DeepLabCut model (Mathis et al. 2018; Figure 3a). We found that both the Stacked Hourglass and Stacked DenseNet models outperformed the LEAP model (Pereira et al., 2019). Notably our Stacked DenseNet model achieved approximately 2x faster inference speeds with 3x higher mean accuracy. Not only were our models' average prediction error significantly improved, but also, importantly, the variance was lower—indicating that our models produced fewer extreme prediction errors. At $\frac{1}{4}$ resolution, our Stacked DenseNet model consistently achieved prediction accuracy nearly identical to the DeepLabCut model (Mathis et al., 2018) while running inference at nearly 2x the speed and using only ~5% of

the parameters—~1.5 million vs. ~26 million. Detailed results of our model comparisons are shown in Figure 3-Figure supplement 1.

While the Stacked DenseNet model used for comparisons is already fast, inference speed could be further improved by using a $\frac{1}{8} \times$ output without much increase in error (Appendix 1 Figure 1) or by further adjusting the hyperparameters to constrain the size of the model. Our Stacked Hourglass implementation followed closely behind the performance of our Stacked DenseNet model and the DeepLabCut model (*Mathis et al., 2018*) but consistently performed more poorly than our Stacked DenseNet model in terms of prediction accuracy, so we excluded this model from further analysis. We were also able to reproduce the results reported by *Pereira et al. (2019)* that the LEAP model and the Stacked Hourglass model (*Newell et al., 2016*) have similar average prediction error for the fly dataset. However, we also find that the LEAP model (*Pereira et al., 2019*) has much higher variance, which suggests it is more prone to extreme prediction errors—a problem for further data analysis.

Stacked DenseNet trains quickly and requires few training examples

To further compare models, we used our zebra dataset to assess the training time needed for our Stacked DenseNet model, the DeepLabCut model (*Mathis et al., 2018*), and the LEAP model (*Pereira et al., 2019*) to reach convergence as well as the amount of training data needed for each model to generalize to new data from outside the training set. We find that our Stacked DenseNet model, the DeepLabCut model (*Mathis et al., 2018*), and the LEAP model (*Pereira et al., 2019*) all fully converge in just a few hours and reach reasonably high accuracy after only an hour of training (Appendix 1 Figure 3). However, it appears that our Stacked DenseNet model tends to converge to a good minimum faster than both the DeepLabCut model (*Mathis et al., 2018*) and the LEAP model (*Pereira et al., 2019*).

We also show that our Stacked DenseNet model achieves good generalization with few training examples and without the use of transfer learning (Appendix 1 Figure 4). These results demonstrate that, when combined with data augmentation, as few as five training examples can be used as an initial training set for labelling keypoints with active learning (Figure 1). Additionally, because our analysis shows that generalization to new data plateaus after approximately 100 labeled training examples, it appears that 100 training examples is a reasonable minimum size for a training set—although the exact number will likely change depending the variance of the image data being annotated. To further examine the effect of transfer learning on model generalization, we compared performance between the DeepLabCut model (*Mathis et al., 2018*) initialized with weights pretrained on the ImageNet database (*Deng et al., 2009*) vs. the same model with randomly-initialized weights (Appendix 1 Figure 4). As postulated by *Mathis et al. (2018)*, we find that transfer learning does provide some benefit to the DeepLabCut model's ability to generalize. However, the effect size of this improvement is small with a mean reduction in Euclidean error of <0.5 pixel. Together these results indicate that transfer learning is helpful, but not required, for deep learning models to achieve good generalization with limited training data.

Discussion

Here we have presented a new software toolkit, called DeepPoseKit, for estimating animal posture using deep learning models. We built on the state-of-the-art for individual pose estimation using convolutional neural networks to achieve fast inference without reducing accuracy or generalization ability. Our new pose estimation model, called Stacked DenseNet, offers considerable improvements (Figure 3a; Figure supplement 1) over the models from *Mathis et al. (2018)* (DeepLabCut) and *Pereira et al. (2019)* (LEAP), and our software framework also provides a simplified interface (Figure 3b) for using these advanced tools to measure animal behavior and locomotion. We tested our methods across a range of datasets from controlled laboratory environments with single individuals to challenging field situations with multiple interacting individuals and variable lighting conditions. We found that our methods perform well for all of these situations and require few training examples to achieve good predictive performance on new data—without the use of transfer learning. We ran experiments to optimize our approach and discovered that some straightforward modifications can greatly improve speed and accuracy. Additionally, we demonstrated that these modifications improve not the just the average error but also help to reduce extreme prediction errors—a key determinant for the reliability of subsequent statistical analysis.

While our results offer a good-faith comparison of the available methods for animal pose estimation, there is inherent uncertainty that we have attempted to account for but may still bias our conclusions. For example, deep learning models are trained using stochastic optimization algorithms that give different results with each replicate, and the Bayesian statistical methods we use for comparison are explicitly probabilistic in nature. There is also great variability across hardware and software configurations when using these models in practice (*Mathis and Warren, 2018*), so performance may change across experimental setups and datasets.

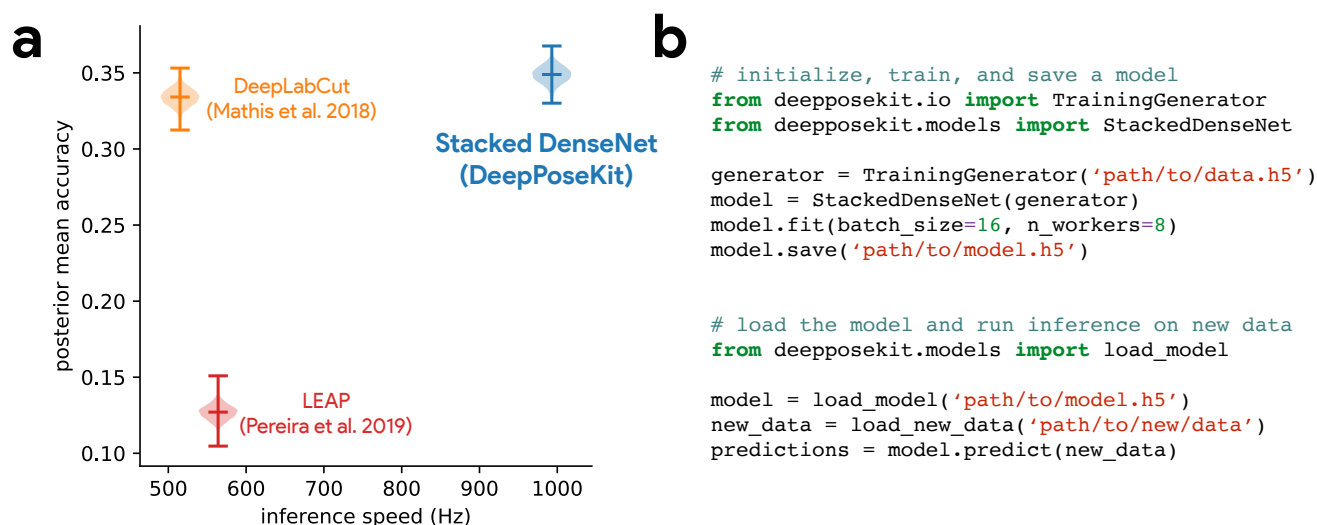


Figure 3. Our Stacked DenseNet model estimates posture at approximately 2x—or greater—the speed of the LEAP model (Pereira et al., 2019) and the DeepLabCut model (Mathis et al., 2018) while also achieving similar accuracy to the DeepLabCut model (Mathis et al., 2018)—shown here as mean accuracy $(1 + \text{Euclidean error})^{-1}$ for our most challenging dataset of multiple interacting Grévy's zebras (*E. grevyi*) recorded in the wild (a). See Figure 3 supplement 1 for further details. Our software interface is designed to be straightforward but flexible. We include many options for expert users to customize model training with sensible default settings to make pose estimation as easy as possible for beginners. For example, training a model and running inference on new data requires writing only a few lines of code and specifying some basic settings (b).

Figure 3—Figure supplement 1. Euclidean error distributions for each model across our three datasets. Letter-value plots (left) show the raw error distributions for each model. Violinplots of the posterior distributions for the mean and variance (right) show statistical differences between the error distributions. Overall the LEAP model (Pereira et al., 2019) was the worst performer on every dataset in terms of both mean and variance. Our Stacked DenseNet model was the best performer for the fly dataset, while our Stacked DenseNet model and the DeepLabCut model (Mathis et al., 2018) both performed equally well on the locust and zebra datasets. The posteriors for the DeepLabCut model (Mathis et al., 2018) and our Stacked DenseNet model are highly overlapping for these datasets, which suggests they are not statistically discernible from one another. Our Stacked Hourglass model (Newell et al., 2016) performed equally to the DeepLabCut model (Mathis et al., 2018) and our Stacked DenseNet model for the locust dataset but performed slightly worse for the fly and zebra datasets.

408 Additionally, we demonstrated that some models may perform better than others for specific applications
409 (Figure 3 supplement 1), and to account for this, our toolkit offers researchers the ability to choose the model
410 that best suits their requirements—including the LEAP model (*Pereira et al., 2019*) and the DeepLabCut model
411 (*Mathis et al., 2018*).

412 We highlighted important considerations when using CNNs for pose estimation and reviewed the progress of
413 fully-convolutional regression models from the literature. The latest advancements for these models have been
414 driven mostly by a strategy of adding more connections between layers to increase performance and efficiency
415 (e.g., *Jégou et al. 2017*). Future progress for this class of models may require better loss functions (*Goodfellow*
416 *et al., 2014*; *Johnson et al., 2016a*; *Chen et al., 2017*; *Zhang et al., 2018*) that more explicitly model the spatial
417 dependencies within a scene, models that incorporate the temporal structure of the data (*Seethapathi et al.,*
418 *2019*), and more mathematically-principled approaches (e.g., *Weigert et al. 2018*; *Roy et al. 2018*) such as the
419 application of formal probabilistic concepts (*Kendall and Gal, 2017*) and Bayesian inference at scale (*Tran et al.,*
420 *2018*).

421 Measuring behavior is a critical factor for many studies in neuroscience (*Krakauer et al., 2017*). Understand-
422 ing the connections between brain activity and behavioral output requires detailed and objective descriptions
423 of body posture that match the richness and resolution neural measurement technologies have provided for
424 years (*Anderson and Perona, 2014*; *Berman, 2018*; *Brown and De Bivort, 2018*), which our methods and other
425 deep-learning-based tools provide (*Mathis et al., 2018*; *Pereira et al., 2019*). We have also demonstrated the
426 possibility that our toolkit could be used for real-time inference, which allows for closed-loop experiments
427 where sensory stimuli or optogenetic stimulation are controlled in response to behavioral measurements
428 (e.g., *Bath et al. 2014*; *Stowers et al. 2017*). Using real-time measurements in conjunction with optogenetics or
429 thermogenetics may be key to disentangling the causal structure of motor output from the brain—especially
430 given that recent work has shown an animal's response to optogenetic stimulation can differ depending on the
431 behavior it is currently performing (*Cande et al., 2018*). Real-time behavioral quantification is also particularly
432 important as closed-loop virtual reality is quickly becoming an indispensable tool for studying sensorimotor
433 relationships in individuals and collectives (*Stowers et al., 2017*).

434 Quantifying individual movement is essential for revealing the genetic (*Kain et al., 2012*; *Brown et al., 2013*;
435 *Ayroles et al., 2015*) and environmental (*Bierbach et al., 2017*; *Akhund-Zade et al., 2019*; *Versace et al., 2019*)
436 underpinnings of phenotypic variation in behavior—as well as the phylogeny of behavior (e.g., *Berman et al.*
437 *2014b*). Measuring individual behavioral phenotypes requires tools that are robust, scaleable, and easy-to-use,
438 and our approach offers the ability to quickly and accurately quantify the behavior of many individuals in
439 great detail. When combined with tools for genetic manipulations (*Ran et al., 2013*; *Doudna and Charpentier,*
440 *2014*), high-throughput behavioral experiments (*Alisch et al., 2018*; *Javer et al., 2018*; *Werkhoven et al., 2019*),
441 and behavioral analysis (e.g., *Berman et al. 2014a*; *Wiltchko et al. 2015*), our methods could help to provide
442 the data resolution and statistical power needed for dissecting the complex relationships between genes,
443 environment, and behavioral variation.

444 When used together with other tools for localization and tracking (e.g., *Pérez-Escudero et al. 2014*; *Crall*
445 *et al. 2015*; *Graving 2017*; *Romero-Ferrero et al. 2019*; *Wild et al. 2018*; *Boenisch et al. 2018*), our methods
446 are capable of reliably measuring posture for multiple interacting individuals. The importance of measuring
447 detailed representations of individual behavior when studying animal collectives has been well established
448 (*Strandburg-Peshkin et al., 2013*; *Rosenthal et al., 2015*; *Strandburg-Peshkin et al., 2015, 2017*). Estimating
449 body posture is an essential first step for unraveling the sensory networks that drive group coordination, such
450 as vision-based networks measured via raycasting (*Strandburg-Peshkin et al., 2013*; *Rosenthal et al., 2015*).
451 Additionally, using body pose estimation in combination with computational models of behavior (e.g., *Costa*
452 *et al. 2019*, *Wiltchko et al. 2015*) and unsupervised behavioral classification methods (e.g., *Berman et al. 2014a,*
453 *Pereira et al. 2019*) may allow for further dissection of how information flows through groups by revealing the
454 networks of behavioral contagion across multiple timescales and sensory modalities. While we have provided a
455 straightforward solution for applying existing pose estimation methods to measure collective behavior, there
456 still remain many challenging scenarios where these methods would fail. For example, tracking posture in a
457 densely-packed bee hive or school of fish would require novel solutions to deal with the 3-D nature of individual
458 movement, which includes maintaining individual identities and dealing with the resulting occlusions that go
459 along with imaging these types of biological systems.

460 When combined with unmanned aerial vehicles (UAVs; *Schiffman 2014*) or other field-based imaging (*Fran-*
461 *cisco et al., 2019*), applying these methods to the study of individuals and groups in the wild can provide
462 high-resolution behavioral data that goes beyond the capabilities of current GPS and accelerometry-based
463 technologies (*Nagy et al., 2010, 2013*; *Kays et al., 2015*; *Strandburg-Peshkin et al., 2015, 2017*; *Flack et al.,*
464 *2018*)—especially for species that are impractical to study with tags or collars. Additionally, by applying these
465 methods in conjunction with 3-D habitat reconstruction—using techniques from photogrammetry (*Strandburg-*

Peshkin et al., 2017; Francisco et al., 2019)—field-based studies can begin to integrate fine-scale behavioral measurements with the full 3-D environment in which the behavior evolved. Future advances will likely allow for the calibration and synchronizaton of imaging devices across multiple UAVs (e.g. *Price et al. 2018; Saini et al. 2019*). This would make it possible to measure the full 3-D posture of wild animals (e.g. *Zuffi et al. 2019*) in scenarios where fixed camera systems (e.g. *Nath et al. 2019*) would not be tractable, such as during migratory or predation events. When combined, these technologies could allow researchers to address questions about the behavioral ecology of animals that were previously impossible to answer.

Computer vision algorithms for measuring behavior at the scale of posture have rapidly advanced in a very short time; nevertheless, the task of pose estimation is far from solved. There are hard limitations to this current generation of pose estimation methods that are primarily related to the requirement for human annotations and user-defined keypoints—both in terms of the number of keypoints, the specific body parts being tracked, and the inherent difficulty of incorporating temporal information into the annotation and training procedure. Often the body parts chosen for annotation are an obvious fit for the experimental design and have reliably-visible reference points on the animal's body that make them easy to annotate. However, in many cases the required number and type of body parts needed for data analysis may not so obvious—such as in the case of unsupervised behavior classification methods (*Berman et al., 2014a; Pereira et al., 2019*). Additionally, the reference points for labeling images with keypoints can be hard to define and consistently annotate across images, which is often the case for soft or flexible-bodied animals like worms and fish. Moreover, due to the laborious nature of annotating keypoints, the current generation of methods also rarely takes into account the natural temporal structure of the data, instead treating each video frame as a statistically independent event, which can lead to extreme prediction errors (reviewed by *Seethapathi et al. 2019*). Extending these methods to track the full three-dimensional posture of animals also typically requires the use of multiple synchronized cameras (*Nath et al., 2019; Günel et al., 2019*), which increases the cost and complexity of creating an experimental setup, as well as the manual labor required for annotating a training set, which must include labeled data from every camera view.

These limitations make it clear that fundamentally-different methods may be required to move the field forward. Future pose estimation methods will likely replace human annotations with fully-articulated volumetric 3-D models of the animal's body (e.g., *Zuffi et al. 2017, 2019*), and the 3-D scene will be learned in an unsupervised or weakly-supervised way (e.g., *Jaques et al. 2019; Zuffi et al. 2019*), where the shape, position, and posture of the animal's body, the camera position and lens parameters, and the background environment and lighting conditions will all be jointly learned directly from 2-D images by a deep-learning model (*Valentin et al., 2019; Zuffi et al., 2019*). These *inverse graphics models* (*Kulkarni et al., 2015; Sabour et al., 2017; Valentin et al., 2019*) will likely take advantage of recently-developed differentiable graphics engines that allow 3-D rendering parameters to be straightforwardly controlled using computationally-efficient optimization methods (*Zuffi et al., 2019; Valentin et al., 2019*). After optimization, the volumetric 3-D timeseries data predicted by the deep learning model could be used directly for behavioral analysis or specific keypoints or body parts could be selected for analysis post-hoc. In order to more explicitly incorporate the natural statistical properties of the data, these models will also likely rely on the use of perceptual (*Johnson et al., 2016a; Zhang et al., 2018; Zuffi et al., 2019*) and adversarial (*Goodfellow et al., 2014; Chen et al., 2017*) loss functions that incorporate spatial dependencies within the scene rather than modelling each video frame as a set of statistically independent pixel distributions—as is the case with current methods that use factorized likelihood functions such as pixel-wise mean squared error (e.g., *Pereira et al. 2019*) or cross-entropy loss (e.g., *Mathis et al. 2018*). Because there would be limited or no requirement for human-provided labels, these models could also be easily modified to incorporate the temporal structure of the data using autoregressive representations (e.g., *Van den Oord et al. 2016; Oord et al. 2016; Kumar et al. 2019*), rather than modeling the scene in each video frame as a statistically independent event. Together these advances could lead to larger, higher-resolution, more reliable behavioral datasets that could revolutionize our understanding of relationships between behavior, the brain, and the environment.

In conclusion, we have presented a new toolkit, called DeepPoseKit, for automatically measuring animal posture from images. We combined recent advances from the literature to create methods that are fast, robust, and widely applicable to a range of species and experimental conditions. When designing our framework we emphasized usability across the entire software interface, which we expect will help to make these advanced tools accessible to a wider range of researchers. The fast inference and real-time capabilities of our methods should also help further reduce barriers to previously intractable questions across many scientific disciplines—including neuroscience, ethology, and behavioral ecology—both in the laboratory and the field.

Methods

We ran three main experiments to test and optimize our approach. First, we compared our new subpixel maxima layer to an integer-based global maxima with downsampled outputs ranging from $1\times$ to $\frac{1}{16}\times$ the input resolution using our Stacked DenseNet model. Next, we tested if training our Stacked DenseNet model to predict the multi-scale geometry of the posture graph improves accuracy. Finally, we compared our model implementations of Stacked Hourglass and Stacked DenseNet to the models from *Pereira et al. (2019)* (LEAP) and *Mathis et al. (2018)* (DeepLabCut), which we also implemented in our framework (see Appendix 8 for details). We assessed both the inference speed and prediction accuracy of each model as well as training time and generalization ability. When comparing these models we incorporated the relevant improvements from our experiments—including subpixel maxima and predicting multi-scale geometry between keypoints—unless otherwise noted (see Appendix 8).

While we do make comparisons to the DeepLabCut model (*Mathis et al., 2018*) we do not use the same training routine as *Mathis et al. (2018)* and *Nath et al. (2019)*, who use binary cross-entropy loss for optimizing the confidence maps in addition to the location refinement maps described by *Insafutdinov et al. (2016)*. We made this modification in order to hold the training routine constant for each model while only varying the model itself. However, we find that these differences between training routines effectively have no impact on performance when the models are trained using the same dataset and data augmentations (Appendix 8 Figure 1). We also provide qualitative comparisons to demonstrate that, when trained with our DeepPoseKit framework, our implementation of the DeepLabCut model (*Mathis et al., 2018*) appears to produce fewer prediction errors than the original implementation from *Mathis et al. (2018)*; *Nath et al. (2019)* when applied to a novel video (Appendix 8 Figure 1-Figure supplements 1 and 2; Appendix 8 Figure 1-video 1).

Datasets

We performed experiments using the vinegar or "fruit" fly (*Drosophila melanogaster*) dataset (Figure 3-video 1) provided by *Pereira et al. (2019)*, and to demonstrate the versatility of our methods we also compared model performance across two previously unpublished posture data sets from groups of desert locusts (*Schistocerca gregaria*) recorded in a laboratory setting (Figure 3-video 2), and herds of Grévy's zebras (*Equus grevyi*) recorded in the wild (Figure 3-video 3). The locust and zebra datasets are particularly challenging for pose estimation as they feature multiple interacting individuals—with focal individuals centered in the frame—and the latter with highly-variable environments and lighting conditions. These datasets are freely-available from <https://github.com/jgraving/deepposekit-data> (*Graving et al., 2019*).

Our locust dataset consisted of a group of 100 locusts in a circular plastic arena 1-m in diameter. The locust group was recorded from above using a high-resolution camera (Basler ace acA2040-90umNIR) and video recording system (Motif, loopbio GmbH). Locusts were localized and tracked using 2-D barcode markers (*Graving, 2017*) attached to the thorax with cyanoacrylate glue, and any missing localizations ($<0.02\%$ of the total dataset) between successful barcode reads were interpolated with linear interpolation. Our zebra dataset consisted of variably sized groups in the wild recorded from above using a commercially-available quadcopter drone (DJI Phantom 4 Pro). Individual zebra were localized using custom deep-learning software based on Faster R-CNN (*Ren et al., 2015*) for predicting bounding boxes. The positions of each zebra were then tracked across frames using a linear assignment algorithm (*Munkres, 1957*) and data were manually verified for accuracy.

After positional tracking, the videos were then cropped using the egocentric coordinates of each individual and saved as separate videos—one for each individual. The images used for each training set were randomly selected using the k-means sampling procedure (with $k=10$) described by *Pereira et al. (2019)* (Appendix 3) to reduce correlation between sampled images. After annotating the images with keypoints, we rotationally and translationally aligned the images and keypoints using the central body axis of the animal in each labeled image. This step allowed us to more easily perform data augmentations (see "Model training") that allow the model to make accurate predictions regardless of the animal's body size and orientation (see Appendix 6). However, this preprocessing step is not a strict requirement for training, and there is no requirement for this preprocessing step when making predictions on new unlabeled data, such as with the methods described by *Pereira et al. (2019)* (Appendix 6). Before training each model we split each annotated dataset into randomly selected training and validation sets with 90% training examples and 10% validation examples, unless otherwise noted. The details for each dataset are described in Table 1.

Model training

For each experiment, we set our model hyperparameters to the same configuration for our Stacked DenseNet and Stacked Hourglass models. Both models were trained with $\frac{1}{4}\times$ resolution outputs and a stack of two networks with two outputs where loss was applied (see Figure 2). Although our model hyperparameters could be infinitely adjusted to trade off between speed and accuracy, we compared only one configuration for each of

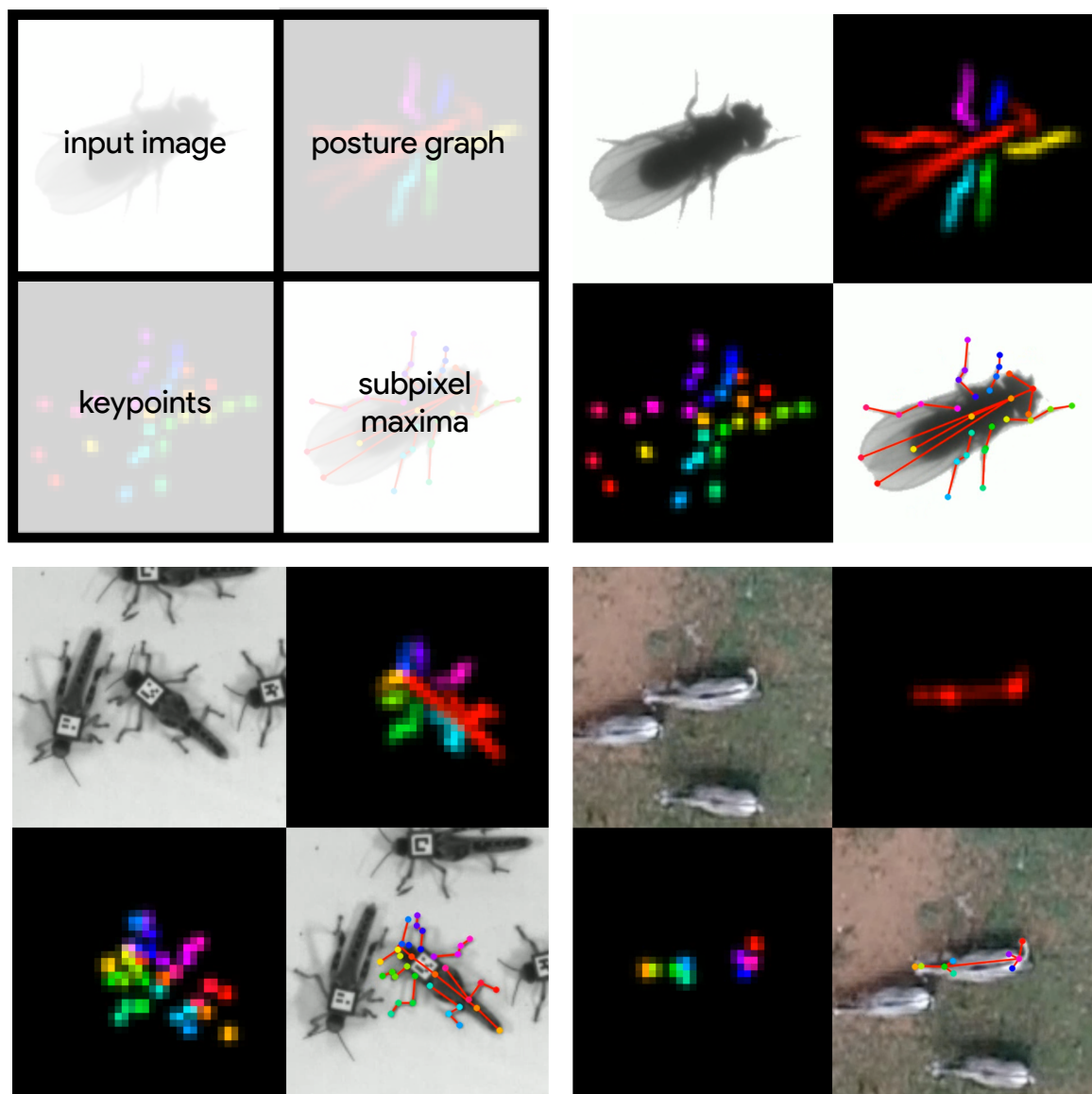


Figure 4. A visualization of the datasets we used to evaluate our methods (Table 1). For each dataset, confidence maps for the keypoints (bottom-left) and posture graph (top-right) are illustrated using different colors for each map. These outputs are from our Stacked DenseNet model at $\frac{1}{4}\times$ resolution.

Figure 4–video 1. A video of a behaving fly from *Pereira et al. (2019)* with pose estimation outputs visualized <https://youtu.be/lsnex6k4NRs>

Figure 4–video 2. A video of a behaving locust with pose estimation outputs visualized. https://youtu.be/b0DyyLP_Czk

Figure 4–video 3. A video of a behaving Grévy's zebra with pose estimation outputs visualized. <https://youtu.be/dSjaphoGHAY>

Table 1. Datasets used for model comparisons.

Name	Species	Resolution	# Images	# Keypoints	Individuals	Source
Vinegar fly	<i>Drosophila melanogaster</i>	192×192	1500	32	Single	<i>Pereira et al. (2019)</i>
Desert locust	<i>Schistocerca gregaria</i>	160×160	800	35	Multiple	This paper
Grévy's zebra	<i>Equus grevyi</i>	160×160	900	9	Multiple	This paper

our model implementations. These results are not meant to be an exhaustive search of model configurations as the best configuration will depend on the application. The details of the hyperparameters we used for each model are described in Appendix 8.

To make our posture estimation tasks closer to realistic conditions, incorporate prior information (Appendix 3), and properly demonstrate the robustness of our methods to rotation, translation, scale, and noise, we applied various augmentations to each data set during training (Figure 2). All models were trained using data augmentations that included random flipping, or mirroring, along both the horizontal and vertical image axes with each axis being independently flipped by drawing from a Bernoulli distribution (with $p = 0.5$); random rotations around the center of the image drawn from a uniform distribution in the range $[-180^\circ, +180^\circ]$; random scaling drawn from a uniform distribution in the range $[90\%, 110\%]$ for flies and locusts and $[75\%, 125\%]$ for zebras (to account for greater size variation in the data set); and random translations along the horizontal and vertical axis independently drawn from a uniform distribution with the range $[-5\%, +5\%]$ —where percentages are relative to the original image size. After performing these spatial augmentations we also applied a variety of noise augmentations that included additive noise—i.e., adding or subtracting randomly-selected values to pixels; dropout—i.e., setting individual pixels or groups of pixels to a randomly-selected value; blurring or sharpening—i.e., changing the composition of spatial frequencies; and contrast ratio augmentations—i.e., changing the ratio between the highest pixel value and lowest pixel value in the image. These augmentations help to further ensure robustness to shifts in lighting, noise, and occlusions. See Appendix 3 for further discussion on data augmentation.

We trained our models (Figure 2) using mean squared error loss optimized using the ADAM optimizer (Kingma and Ba, 2014) with a learning rate of 1×10^{-3} and a batch size of 16. We lowered the learning rate by a factor of 5 each time the validation loss did not improve by more than 1×10^{-3} for 10 epochs. We considered models to be converged when the validation loss stopped improving for 50 epochs, and we calculated validation error as the Euclidean distance between predicted and ground-truth image coordinates for only the best performing version of the model, which we evaluated at the end of each epoch during optimization. We performed this procedure five times for each experiment and randomly selected a new validation set for each replicate.

Model evaluation

Machine learning models are typically evaluated for their ability to generalize to new data, known as *predictive performance*, using a held-out *test set*—a subsample of annotated data that is not used for training or validation. However, due to the small size of the datasets used for making comparisons, we elected to use only a validation set for model evaluation, as using an overly small training or test set can bias assessments of a model's predictive performance (Kuhn and Johnson, 2013). Generally a test set is used to avoid biased performance measures caused by overfitting the model hyperparameters to the validation set. However, we did not adjust our model architecture to achieve better performance on our validation set—only to achieve fast inference speeds. While we did use validation error to decide when to lower the learning rate during training and when to stop training, lowering the learning rate in this way should have no effect on the generalization ability of the model, and because we heavily augment our training set during optimization—forcing the model to learn a much larger data distribution than what is included in the training and validation sets—overfitting to the validation set is unlikely. We also demonstrate the generality of our results for each experiment by randomly selecting a new validation set with each replicate. All of these factors make the Euclidean error for the unaugmented validation set a reasonable measure of the predictive performance for each model.

The inference speed for each model was assessed by running predictions on 100,000 randomly generated images with a batch size of 1 for real-time speeds and a batch size of 100 for offline speeds, unless otherwise noted. Our hardware consisted of a Dell Precision Tower 7910 workstation (Dell, Inc.) running Ubuntu Linux v18.04 with 2x Intel Xeon E5-2623 v3 CPUs (8 cores, 16 threads at 3.00GHz), 64GB of RAM, a Quadro P6000 GPU and a Titan Xp GPU (NVIDIA Corporation). We used both GPUs (separately) for training models and evaluating predictive performance, but we only used the faster Titan Xp GPU for benchmarking inference speeds and training time. While the hardware we used for development and testing is on the high-end of the current performance spectrum, there is no requirement for this level of performance, and our software can easily be run on lower-end hardware. We evaluated inference speeds on multiple consumer-grade desktop computers and found similar performance ($\pm 10\%$) when using the same GPU; however, training speed depends more heavily on other hardware components like the CPU and hard disk.

Assessing prediction accuracy with Bayesian inference

To more rigorously assess performance differences between models, we parameterized the Euclidean error distribution for each experiment by fitting a Bayesian linear model with a Gamma-distributed likelihood function.

633 This model takes the form:

$$\begin{aligned} p(y|X, \theta_\mu, \theta_\phi) &\sim \text{Gamma}(\alpha, \beta) \\ \alpha &= \mu^2 \phi^{-1} \\ \beta &= \mu \phi^{-1} \\ \mu &= h(X\theta_\mu) \\ \phi &= h(X\theta_\phi) \end{aligned}$$

634 where X is the design matrix composed of binary indicator variables for each pose estimation model, θ_μ
635 and θ_ϕ are vectors of intercepts, $h(\cdot)$ is the softplus function (Dugas et al., 2001)—or $h(x) = \log(1 + e^x)$ —used to
636 enforce positivity of μ and ϕ , and y is the Euclidean error of the pose estimation model. Parameterizing our
637 error distributions in this way allows us to calculate the posterior distributions for the mean $E[y] = \alpha\beta^{-1} \equiv \mu$ and
638 variance $\text{Var}[y] = \alpha\beta^{-2} \equiv \phi$. This parameterization then provides us with a statistically rigorous way to assess
639 differences in model accuracy in terms of both central tendency and spread—accounting for both epistemic
640 uncertainty (unknown unknowns; e.g., parameter uncertainty) and aleatoric uncertainty (known unknowns; e.g.,
641 data variance). Details of how we fitted these models can be found in Appendix 7.

642 Author contributions

643 J.M.G. and I.D.C. conceived the idea for the project. J.M.G. and D.C. developed the software with input from H.N.
644 J.M.G. implemented the pose estimation models and developed the subpixel maxima algorithm. J.M.G. and D.C.
645 developed the annotation GUI, data augmentation pipeline, and wrote the documentation. J.M.G., D.C. and H.N.
646 designed the experiments. J.M.G. and D.C. ran the experiments. B.R.C., B.K., J.M.G., and I.D.C. conceived the idea
647 to apply posture tracking to zebras. B.R.C. and B.K. provided the annotated zebra posture data. B.K., and L.L.
648 helped with initial testing and improvement of the software interface. L.L. also made significant contributions to
649 an earlier version of the manuscript. J.M.G. fit the linear models and made the figures. J.M.G. wrote the initial
650 draft of the manuscript with input from H.N. and D.C., and all authors helped revise the manuscript.

651 Acknowledgements

652 We are indebted to Talmo Pereira et al. and A. Mathis et al. for making their software open-source and
653 freely-available—this project would not have been possible without them. We also thank M. Mathis and A.
654 Mathis for their comments, which greatly improved the manuscript. We thank François Chollet, the Keras
655 and TensorFlow teams, and Alexander Jung for their open source contributions, which provided the core
656 programming interface for our work. We thank A. Strandburg-Peshkin, Vivek H. Sridhar, Michael L. Smith, and
657 Joseph B. Bak-Coleman for their helpful discussions on the project and comments on the manuscript. We
658 also thank M.L.S. for the use of his GPU. We thank Felicitas Oehler for annotating the zebra posture data and
659 Chiara Hirschhorn for assistance with filming the locusts and annotating the locust posture data. We thank
660 Alex Bruttel, Christine Bauer, Jayme Weglarski, Dominique Leo, Markus Miller and loobio GmbH for providing
661 technical support. We acknowledge the NVIDIA Corporation for their generous donations to our research. This
662 project received funding from the European Union's Horizon 2020 research and innovation programme under
663 the Marie Skłodowska-Curie grant agreement No. 748549. B.R.C. acknowledges support from the University
664 of Konstanz Zukunftskolleg's Investment Grant program. I.D.C. acknowledges support from NSF Grant IOS-
665 1355061, Office of Naval Research Grants N00014-09-1-1074 and N00014-14-1-0635, Army Research Office
666 Grants W911NG-11-1-0385 and W911NF14-1-0431, the Struktur-und Innovationsfonds für die Forschung of the
667 State of Baden-Württemberg, the DFG Centre of Excellence 2117 "Centre for the Advanced Study of Collective
668 Behaviour" (ID: 422037984), and the Max Planck Society.

669 Animal Ethics Statement

670 All procedures for collecting the zebra (*E. grevyi*) dataset were reviewed and approved by Ethikrat, the inde-
671 pendent Ethics Council of the Max Planck Society. The zebra dataset was collected with the permission of
672 Kenya's National Commission for Science, Technology and Innovation (NACOSTI/P/17/59088/15489 and NA-
673 COSTI/P/18/59088/21567) using drones operated by B.R.C. with the permission of the Kenya Civil Aviation
674 Authority (authorization numbers: KCAA/OPS/2117/4 Vol. 2 (80), KCAA/OPS/2117/4 Vol. 2 (81), KCAA/OPS/2117/5
675 (86) and KCAA/OPS/2117/5 (87); RPAS Operator Certificate numbers: RPA/TP/0005 AND RPA/TP/000-0009).

References

- 676 **References**
- 677 **Abadi M**, Agarwal A, Barham P, Brevdo E, Chen Z, Citro C, Corrado GS, Davis A, Dean J, Devin M, Ghemawat S, Goodfellow I, Harp
678 A, Irving G, Isard M, Jia Y, Jozefowicz R, Kaiser L, Kudlur M, Levenberg J, et al., TensorFlow: Large-Scale Machine Learning on
679 Heterogeneous Systems; 2015. <https://www.tensorflow.org/>, software available from tensorflow.org.
- 680 **Akhund-Zade J**, Ho S, O'Leary C, de Bivort B. The effect of environmental enrichment on behavioral variability depends on
681 genotype, behavior, and type of enrichment. *Journal of Experimental Biology*. 2019; [https://jeb.biologists.org/content/early/](https://jeb.biologists.org/content/early/2019/08/14/jeb.202234)
682 [2019/08/14/jeb.202234](https://jeb.biologists.org/content/early/2019/08/14/jeb.202234), doi: 10.1242/jeb.202234.
- 683 **Alisch T**, Crall JD, Kao AB, Zucker D, de Bivort BL. MAPLE (modular automated platform for large-scale experiments), a robot for
684 integrated organism-handling and phenotyping. *eLife*. 2018; 7:e37166.
- 685 **Anderson DJ**, Perona P. Toward a science of computational ethology. *Neuron*. 2014; 84(1):18–31.
- 686 **Andriluka M**, Iqbal U, Insafutdinov E, Pishchulin L, Milan A, Gall J, Schiele B. PoseTrack: A benchmark for human pose estimation
687 and tracking. In: *Proceedings of the IEEE Conference on Computer Vision and Pattern Recognition*; 2018. p. 5167–5176.
- 688 **Andriluka M**, Pishchulin L, Gehler P, Schiele B. 2D Human Pose Estimation: New Benchmark and State of the Art Analysis. In:
689 *IEEE Conference on Computer Vision and Pattern Recognition (CVPR)*; 2014. .
- 690 **Ayinde BO**, Zurada JM. Building efficient convnets using redundant feature pruning. *arXiv preprint arXiv:180207653*. 2018; .
- 691 **Ayroles JF**, Buchanan SM, O'Leary C, Skutt-Kakaria K, Grenier JK, Clark AG, Hartl DL, de Bivort BL. Behavioral idiosyncrasy reveals
692 genetic control of phenotypic variability. *Proceedings of the National Academy of Sciences*. 2015; 112(21):6706–6711.
- 693 **Badrinarayanan V**, Kendall A, Cipolla R. SegNet: A Deep Convolutional Encoder-Decoder Architecture for Image Segmentation.
694 CoRR. 2015; abs/1511.00561. <http://arxiv.org/abs/1511.00561>.
- 695 **Bath DE**, Stowers JR, Hörmann D, Poehlmann A, Dickson BJ, Straw AD. FlyMAD: rapid thermogenetic control of neuronal activity
696 in freely walking *Drosophila*. *Nature methods*. 2014; 11(7):756.
- 697 **Berman GJ**. Measuring behavior across scales. *BMC biology*. 2018; 16(1):23.
- 698 **Berman GJ**, Bialek W, Shaevitz JW. Predictability and hierarchy in *Drosophila* behavior. *Proceedings of the National Academy of*
699 *Sciences*. 2016; 113(42):11943–11948.
- 700 **Berman GJ**, Choi DM, Bialek W, Shaevitz JW. Mapping the stereotyped behaviour of freely moving fruit flies. *Journal of The Royal*
701 *Society Interface*. 2014; 11(99):20140672.
- 702 **Berman GJ**, Choi DM, Bialek W, Shaevitz JW. Mapping the structure of drosophilid behavior. *bioRxiv*. 2014; p. 002873.
- 703 **Bierbach D**, Laskowski KL, Wolf M. Behavioural individuality in clonal fish arises despite near-identical rearing conditions.
704 *Nature communications*. 2017; 8:15361.
- 705 **Boenisch F**, Rosemann B, Wild B, Dormagen D, Wario F, Landgraf T. Tracking All Members of a Honey Bee Colony Over Their
706 Lifetime Using Learned Models of Correspondence. *Frontiers in Robotics and AI*. 2018; 5:35. [https://www.frontiersin.org/](https://www.frontiersin.org/article/10.3389/frobt.2018.00035)
707 [article/10.3389/frobt.2018.00035](https://www.frontiersin.org/article/10.3389/frobt.2018.00035), doi: 10.3389/frobt.2018.00035.
- 708 **Brown AE**, De Bivort B. Ethology as a physical science. *Nature Physics*. 2018; p. 1.
- 709 **Brown AE**, Yemini EI, Grundy LJ, Jucikas T, Schafer WR. A dictionary of behavioral motifs reveals clusters of genes affecting
710 *Caenorhabditis elegans* locomotion. *Proceedings of the National Academy of Sciences*. 2013; 110(2):791–796.
- 711 **Cande J**, Namiki S, Qiu J, Korff W, Card GM, Shaevitz JW, Stern DL, Berman GJ. Optogenetic dissection of descending behavioral
712 control in *Drosophila*. *Elife*. 2018; 7:e34275.
- 713 **Cao Z**, Simon T, Wei SE, Sheikh Y. Realtime multi-person 2d pose estimation using part affinity fields. In: *Proceedings of the IEEE*
714 *Conference on Computer Vision and Pattern Recognition*; 2017. p. 7291–7299.
- 715 **Carpenter B**, Lee D, Brubaker MA, Riddell A, Gelman A, Goodrich B, Guo J, Hoffman M, Betancourt M, Li P. Stan: A Probabilistic
716 Programming Language. *J Stat Softw*. 2017; .
- 717 **Cauchy A**. Méthode générale pour la résolution des systemes d'équations simultanées. *Comp Rend Sci Paris*. 1847; 25(1847):536–
718 538.
- 719 **Chen Y**, Shen C, Wei XS, Liu L, Yang J. Adversarial poseNet: A structure-aware convolutional network for human pose estimation.
720 In: *Proceedings of the IEEE International Conference on Computer Vision*; 2017. p. 1212–1221.
- 721 **Chollet F**, et al., Keras. GitHub; 2015. <https://github.com/fchollet/keras>.
- 722 **Chollet F**. Xception: Deep learning with depthwise separable convolutions. In: *Proceedings of the IEEE conference on computer*
723 *vision and pattern recognition*; 2017. p. 1251–1258.

Costa AC, Ahamed T, Stephens GJ. Adaptive, locally linear models of complex dynamics. *Proceedings of the National Academy of Sciences*. 2019; 116(5):1501–1510. <https://www.pnas.org/content/116/5/1501>, doi: 10.1073/pnas.1813476116.

Crall JD, Gravish N, Mountcastle AM, Combes SA. BEETag: a low-cost, image-based tracking system for the study of animal behavior and locomotion. *PloS one*. 2015; 10(9):e0136487.

Dell AI, Bender JA, Branson K, Couzin ID, de Polavieja GG, Noldus LP, Pérez-Escudero A, Perona P, Straw AD, Wikelski M, et al. Automated image-based tracking and its application in ecology. *Trends in ecology & evolution*. 2014; 29(7):417–428.

Deng J, Dong W, Socher R, Li LJ, Li K, Fei-Fei L. Imagenet: A large-scale hierarchical image database. . 2009; .

Doudna JA, Charpentier E. The new frontier of genome engineering with CRISPR-Cas9. *Science*. 2014; 346(6213):1258096.

Duane S, Kennedy AD, Pendleton BJ, Roweth D. Hybrid Monte Carlo. *Phys Lett B*. 1987; 195(2):216–222.

Dugas C, Bengio Y, Bélisle F, Nadeau C, Garcia R. Incorporating second-order functional knowledge for better option pricing. In: *Advances in neural information processing systems*; 2001. p. 472–478.

Flack A, Nagy M, Fiedler W, Couzin ID, Wikelski M. From local collective behavior to global migratory patterns in white storks. *Science*. 2018; 360(6391):911–914.

Francisco FA, Nührenberg P, Jordan AL. A low-cost, open-source framework for tracking and behavioural analysis of animals in aquatic ecosystems. *bioRxiv*. 2019; <https://www.biorxiv.org/content/early/2019/03/09/571232>, doi: 10.1101/571232.

Goodfellow I, Bengio Y, Courville A. *Deep learning*. MIT press; 2016.

Goodfellow I, Pouget-Abadie J, Mirza M, Xu B, Warde-Farley D, Ozair S, Courville A, Bengio Y. Generative adversarial nets. In: *Advances in neural information processing systems*; 2014. p. 2672–2680.

Graving JM, pinpoint: behavioral tracking using 2D barcode tags v0.0.1-alpha; 2017. <https://doi.org/10.5281/zenodo.1008970>, doi: 10.5281/zenodo.1008970.

Graving JM, Chae D, Naik H, Li L, Koger B, Costelloe BR, Couzin ID, Example Datasets for DeepPoseKit; 2019. <https://doi.org/10.5281/zenodo.3366908>, doi: 10.5281/zenodo.3366908.

Guizar-Sicairos M, Thurman ST, Fienup JR. Efficient subpixel image registration algorithms. *Optics letters*. 2008; 33(2):156–158.

Günel S, Rhodin H, Morales D, Campagnolo J, Ramdya P, Fua P. DeepFly3D: A deep learning-based approach for 3D limb and appendage tracking in tethered, adult Drosophila. *bioRxiv*. 2019; p. 640375.

He K, Zhang X, Ren S, Sun J. Deep residual learning for image recognition. In: *Proceedings of the IEEE conference on computer vision and pattern recognition*; 2016. p. 770–778.

Hoffman MD, Gelman A. The No-U-Turn sampler: adaptively setting path lengths in Hamiltonian Monte Carlo. *Journal of Machine Learning Research*. 2014; 15(1):1593–1623.

Huang G, Liu Z, Van Der Maaten L, Weinberger KQ. Densely connected convolutional networks. In: *Proceedings of the IEEE conference on computer vision and pattern recognition*; 2017. p. 4700–4708.

Huang J, Rathod V, Sun C, Zhu M, Korattikara A, Fathi A, Fischer I, Wojna Z, Song Y, Guadarrama S, et al. Speed/accuracy trade-offs for modern convolutional object detectors. In: *Proceedings of the IEEE conference on computer vision and pattern recognition*; 2017. p. 7310–7311.

Insafutdinov E, Pishchulin L, Andres B, Andriluka M, Schiele B. Deeppercut: A deeper, stronger, and faster multi-person pose estimation model. In: *European Conference on Computer Vision* Springer; 2016. p. 34–50.

Iqbal U, Milan A, Gall J. Posetrack: Joint multi-person pose estimation and tracking. In: *Proceedings of the IEEE Conference on Computer Vision and Pattern Recognition*; 2017. p. 2011–2020.

Jaques M, Burke M, Hospedales T. Physics-as-Inverse-Graphics: Joint Unsupervised Learning of Objects and Physics from Video. *arXiv preprint arXiv:1905.11169*. 2019; .

Javer A, Currie M, Lee CW, Hokanson J, Li K, Martineau CN, Yemini E, Grundy LJ, Li C, Ch'ng Q, et al. An open-source platform for analyzing and sharing worm-behavior data. *Nature methods*. 2018; 15(9):645.

Jégou S, Drozdal M, Vázquez D, Romero A, Bengio Y. The One Hundred Layers Tiramisu: Fully Convolutional DenseNets for Semantic Segmentation. *CoRR*. 2017; abs/1611.09326. <http://arxiv.org/abs/1611.09326>.

Johnson J, Alahi A, Fei-Fei L. Perceptual losses for real-time style transfer and super-resolution. In: *European conference on computer vision* Springer; 2016. p. 694–711.

Johnson M, Duvenaud DK, Wiltchko A, Adams RP, Datta SR. Composing graphical models with neural networks for structured representations and fast inference. In: *Advances in neural information processing systems*; 2016. p. 2946–2954.

772 Jolles JW, Boogert NJ, Sridhar VH, Couzin ID, Manica A. Consistent individual differences drive collective behavior and group
773 functioning of schooling fish. *Current Biology*. 2017; 27(18):2862–2868.

774 Jung A, imgaug. GitHub; 2018. <https://github.com/aleju/imgaug>.

775 Kain J, Stokes C, Gaudry Q, Song X, Foley J, Wilson R, De Bivort B. Leg-tracking and automated behavioural classification in
776 *Drosophila*. *Nature communications*. 2013; 4:1910.

777 Kain JS, Stokes C, de Bivort BL. Phototactic personality in fruit flies and its suppression by serotonin and white. *Proceedings of*
778 *the National Academy of Sciences*. 2012; 109(48):19834–19839.

779 Kays R, Crofoot MC, Jetz W, Wikelski M. Terrestrial animal tracking as an eye on life and planet. *Science*. 2015; 348(6240):aaa2478.

780 Ke L, Chang MC, Qi H, Lyu S. Multi-Scale Structure-Aware Network for Human Pose Estimation. In: *The European Conference on*
781 *Computer Vision (ECCV)*; 2018. .

782 Kendall A, Gal Y. What uncertainties do we need in bayesian deep learning for computer vision? In: *Advances in neural*
783 *information processing systems*; 2017. p. 5574–5584.

784 Kiefer J, Wolfowitz J, et al. Stochastic estimation of the maximum of a regression function. *The Annals of Mathematical Statistics*.
785 1952; 23(3):462–466.

786 Kingma DP, Ba J. Adam: A method for stochastic optimization. *arXiv preprint arXiv:1412.6980*. 2014; .

787 Klambauer G, Unterthiner T, Mayr A, Hochreiter S. Self-normalizing neural networks. In: *Advances in neural information*
788 *processing systems*; 2017. p. 971–980.

789 Klibaite U, Berman GJ, Cande J, Stern DL, Shaevitz JW. An unsupervised method for quantifying the behavior of paired animals.
790 *Physical biology*. 2017; 14(1):015006.

791 Klibaite U, Shaevitz JW. Interacting fruit flies synchronize behavior. *bioRxiv*. 2019; p. 545483.

792 Krakauer JW, Ghazanfar AA, Gomez-Marín A, MacIver MA, Poeppel D. Neuroscience needs behavior: correcting a reductionist
793 bias. *Neuron*. 2017; 93(3):480–490.

794 Kuhn M, Johnson K. *Applied predictive modeling*, vol. 26. Springer; 2013.

795 Kulkarni TD, Whitney WF, Kohli P, Tenenbaum J. Deep convolutional inverse graphics network. In: *Advances in neural information*
796 *processing systems*; 2015. p. 2539–2547.

797 Kumar M, Babaeizadeh M, Erhan D, Finn C, Levine S, Dinh L, Kingma D. VideoFlow: A flow-based generative model for video.
798 *arXiv preprint arXiv:1903.01434*. 2019; .

799 LeCun Y, Bengio Y, Hinton G. Deep learning. *nature*. 2015; 521(7553):436.

800 Li H, Xu Z, Taylor G, Studer C, Goldstein T. Visualizing the loss landscape of neural nets. In: *Advances in Neural Information*
801 *Processing Systems*; 2018. p. 6391–6401.

802 Long J, Shelhamer E, Darrell T. Fully convolutional networks for semantic segmentation. In: *Proceedings of the IEEE conference on*
803 *computer vision and pattern recognition*; 2015. p. 3431–3440.

804 Markowitz JE, Gillis WF, Beron CC, Neufeld SQ, Robertson K, Bhagat ND, Peterson RE, Peterson E, Hyun M, Linderman SW, et al.
805 The striatum organizes 3D behavior via moment-to-moment action selection. *Cell*. 2018; 174(1):44–58.

806 Mathis A, Mamidanna P, Cury KM, Abe T, Murthy VN, Mathis MW, Bethge M. DeepLabCut: markerless pose estimation of user-
807 defined body parts with deep learning. *Nature Neuroscience*. 2018; <https://www.nature.com/articles/s41593-018-0209-y>.

808 Mathis A, Warren RA. On the inference speed and video-compression robustness of DeepLabCut. *bioRxiv*. 2018; <https://www.biorxiv.org/content/early/2018/10/30/457242>, doi: 10.1101/457242.

810 Mendes CS, Bartos I, Akay T, Márka S, Mann RS. Quantification of gait parameters in freely walking wild type and sensory
811 deprived *Drosophila melanogaster*. *elife*. 2013; 2:e00231.

812 Munkres J. Algorithms for the assignment and transportation problems. *Journal of the society for industrial and applied*
813 *mathematics*. 1957; 5(1):32–38.

814 Nagy M, Akos Z, Biro D, Vicsek T. Hierarchical group dynamics in pigeon flocks. *Nature*. 2010; 464(7290):890.

815 Nagy M, Vászárhelyi G, Pettit B, Roberts-Mariani I, Vicsek T, Biro D. Context-dependent hierarchies in pigeons. *Proceedings of the*
816 *National Academy of Sciences*. 2013; 110(32):13049–13054.

817 Nath T, Mathis A, Chen AC, Patel A, Bethge M, Mathis MW. Using DeepLabCut for 3D markerless pose estimation across species
818 and behaviors. *Nature protocols*. 2019; .

819 **Newell A**, Yang K, Deng J. Stacked Hourglass Networks for Human Pose Estimation. In: *Computer Vision - ECCV 2016 -*
820 *14th European Conference, Amsterdam, The Netherlands, October 11-14, 2016, Proceedings, Part VIII*; 2016. p. 483–499. doi:
821 10.1007/978-3-319-46484-8_29.

822 **Van den Oord A**, Kalchbrenner N, Espeholt L, Vinyals O, Graves A, et al. Conditional image generation with pixelcnn decoders.
823 In: *Advances in neural information processing systems*; 2016. p. 4790–4798.

824 **Oord Avd**, Dieleman S, Zen H, Simonyan K, Vinyals O, Graves A, Kalchbrenner N, Senior A, Kavukcuoglu K. Wavenet: A generative
825 model for raw audio. arXiv preprint arXiv:160903499. 2016; .

826 **Pereira TD**, Aldarondo DE, Willmore L, Kislin M, Wang SSH, Murthy M, Shaevitz JW. Fast animal pose estimation using deep
827 neural networks. *Nature methods*. 2019; 16(1):117.

828 **Pérez-Escudero A**, Vicente-Page J, Hinz RC, Arganda S, De Polavieja GG. idTracker: tracking individuals in a group by automatic
829 identification of unmarked animals. *Nature methods*. 2014; 11(7):743.

830 **Pratt LY**. Discriminability-based transfer between neural networks. In: *Advances in neural information processing systems*; 1993.
831 p. 204–211.

832 **Prechelt L**. Automatic early stopping using cross validation: quantifying the criteria. *Neural Networks*. 1998; 11(4):761–767.

833 **Price E**, Lawless G, Ludwig R, Martinovic I, Bühlhoff HH, Black MJ, Ahmad A. Deep neural network-based cooperative visual
834 tracking through multiple micro aerial vehicles. *IEEE Robotics and Automation Letters*. 2018; 3(4):3193–3200.

835 **Ran FA**, Hsu PD, Wright J, Agarwala V, Scott DA, Zhang F. Genome engineering using the CRISPR-Cas9 system. *Nature protocols*.
836 2013; 8(11):2281.

837 **Ren S**, He K, Girshick R, Sun J. Faster r-cnn: Towards real-time object detection with region proposal networks. In: *Advances in*
838 *neural information processing systems*; 2015. p. 91–99.

839 **Robbins H**, Monro S. A stochastic approximation method. *The annals of mathematical statistics*. 1951; p. 400–407.

840 **Romero-Ferrero F**, Bergomi MG, Hinz RC, Heras FJ, de Polavieja GG. idtracker. ai: tracking all individuals in small or large
841 collectives of unmarked animals. *Nature methods*. 2019; 16(2):179.

842 **Ronneberger O**, Fischer P, Brox T. U-net: Convolutional networks for biomedical image segmentation. In: *International*
843 *Conference on Medical image computing and computer-assisted intervention* Springer; 2015. p. 234–241.

844 **Rosenthal SB**, Twomey CR, Hartnett AT, Wu HS, Couzin ID. Revealing the hidden networks of interaction in mobile animal groups
845 allows prediction of complex behavioral contagion. *Proceedings of the National Academy of Sciences*. 2015; 112(15):4690–
846 4695.

847 **Roy AG**, Conjeti S, Navab N, Wachinger C. Bayesian QuickNAT: Model Uncertainty in Deep Whole-Brain Segmentation for
848 Structure-wise Quality Control. CoRR. 2018; abs/1811.09800. <http://arxiv.org/abs/1811.09800>.

849 **Sabour S**, Frosst N, Hinton GE. Dynamic routing between capsules. In: *Advances in neural information processing systems*; 2017.
850 p. 3856–3866.

851 **Saini N**, Price E, Tallamraju R, Enfiacud R, Ludwig R, Martinovič I, Ahmad A, Black M. Markerless Outdoor Human Motion
852 Capture Using Multiple Autonomous Micro Aerial Vehicles. In: *International Conference on Computer Vision*; 2019. .

853 **Sandler M**, Howard A, Zhu M, Zhmoginov A, Chen LC. Mobilenetv2: Inverted residuals and linear bottlenecks. In: *Proceedings of*
854 *the IEEE Conference on Computer Vision and Pattern Recognition*; 2018. p. 4510–4520.

855 **Schiffman R**. Drones flying high as new tool for field biologists. *American Association for the Advancement of Science*; 2014.

856 **Seethapathi N**, Wang S, Saluja R, Blohm G, Kording KP. Movement science needs different pose tracking algorithms. arXiv
857 preprint arXiv:190710226. 2019; .

858 **Stephens GJ**, de Mesquita MB, Ryu WS, Bialek W. Emergence of long timescales and stereotyped behaviors in *Caenorhabditis*
859 *elegans*. *Proceedings of the National Academy of Sciences*. 2011; 108(18):7286–7289.

860 **Stowers JR**, Hofbauer M, Bastien R, Griessner J, Higgins P, Farooqui S, Fischer RM, Nowikovsky K, Haubensak W, Couzin ID, et al.
861 Virtual reality for freely moving animals. *Nature methods*. 2017; 14(10):995.

862 **Strandburg-Peshkin A**, Farine DR, Couzin ID, Crofoot MC. Shared decision-making drives collective movement in wild baboons.
863 *Science*. 2015; 348(6241):1358–1361.

864 **Strandburg-Peshkin A**, Farine DR, Crofoot MC, Couzin ID. Habitat and social factors shape individual decisions and emergent
865 group structure during baboon collective movement. *Elife*. 2017; 6:e19505.

866 **Strandburg-Peshkin A**, Twomey CR, Bode NW, Kao AB, Katz Y, Ioannou CC, Rosenthal SB, Torney CJ, Wu HS, Levin SA, et al.
867 Visual sensory networks and effective information transfer in animal groups. *Current Biology*. 2013; 23(17):R709–R711.

868 **Todd JG**, Kain JS, de Bivort BL. Systematic exploration of unsupervised methods for mapping behavior. *Physical biology*. 2017;
869 14(1):015002.

870 **Tran D**, Hoffman MW, Moore D, Suter C, Vasudevan S, Radul A. Simple, distributed, and accelerated probabilistic programming.
871 In: *Advances in Neural Information Processing Systems*; 2018. p. 7609–7620.

872 **Uhlmann V**, Ramdya P, Delgado-Gonzalo R, Benton R, Unser M. FlyLimbTracker: An active contour based approach for leg
873 segment tracking in unmarked, freely behaving *Drosophila*. *PLoS One*. 2017; 12(4):e0173433.

874 **Valentin J**, Keskin C, Pidlypenskyi P, Makadia A, Sud A, Bouaziz S. TensorFlow Graphics: Computer Graphics Meets Deep
875 Learning. In: ; 2019. .

876 **Versace E**, Caffini M, Werkhoven Z, de Bivort BL. Individual, but not population asymmetries, are modulated by social
877 environment and genotype in *Drosophila melanogaster*. *bioRxiv*. 2019; p. 694901.

878 **Weigert M**, Schmidt U, Boothe T, Müller A, Dibrov A, Jain A, Wilhelm B, Schmidt D, Broaddus C, Culley S, et al. Content-aware
879 image restoration: pushing the limits of fluorescence microscopy. *Nature methods*. 2018; 15(12):1090.

880 **Werkhoven Z**, Rohrsen C, Qin C, Brembs B, de Bivort B. MARGO (Massively Automated Real-time GUI for Object-tracking), a
881 platform for high-throughput ethology. *BioRxiv*. 2019; p. 593046.

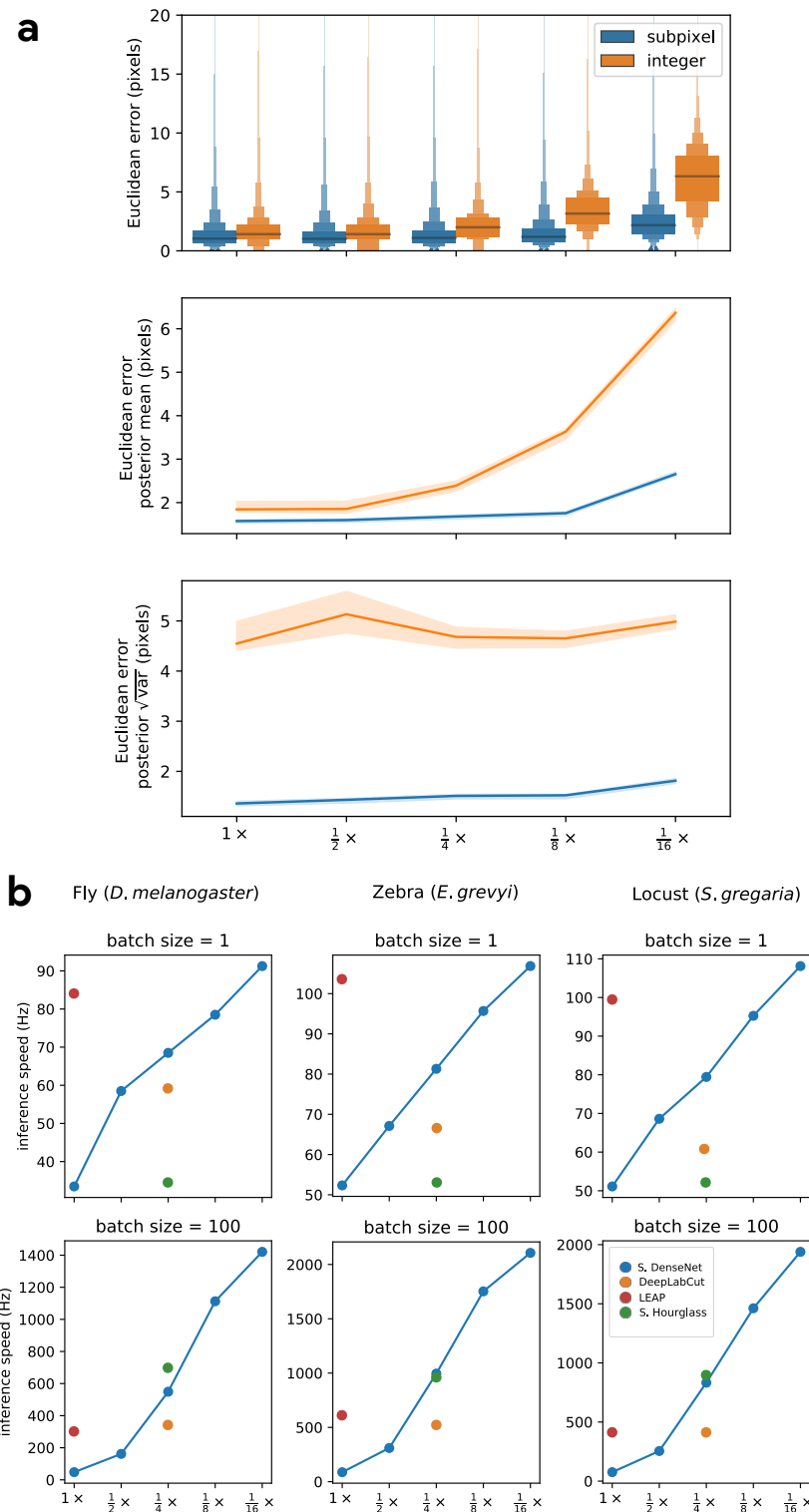
882 **Wild B**, Sixt L, Landgraf T. Automatic localization and decoding of honeybee markers using deep convolutional neural networks.
883 *CoRR*. 2018; abs/1802.04557. <http://arxiv.org/abs/1802.04557>.

884 **Wiltchko AB**, Johnson MJ, Iurilli G, Peterson RE, Katon JM, Pashkovski SL, Abaira VE, Adams RP, Datta SR. Mapping sub-second
885 structure in mouse behavior. *Neuron*. 2015; 88(6):1121–1135.

886 **Zhang R**, Isola P, Efros AA, Shechtman E, Wang O. The unreasonable effectiveness of deep features as a perceptual metric. In:
887 *Proceedings of the IEEE Conference on Computer Vision and Pattern Recognition*; 2018. p. 586–595.

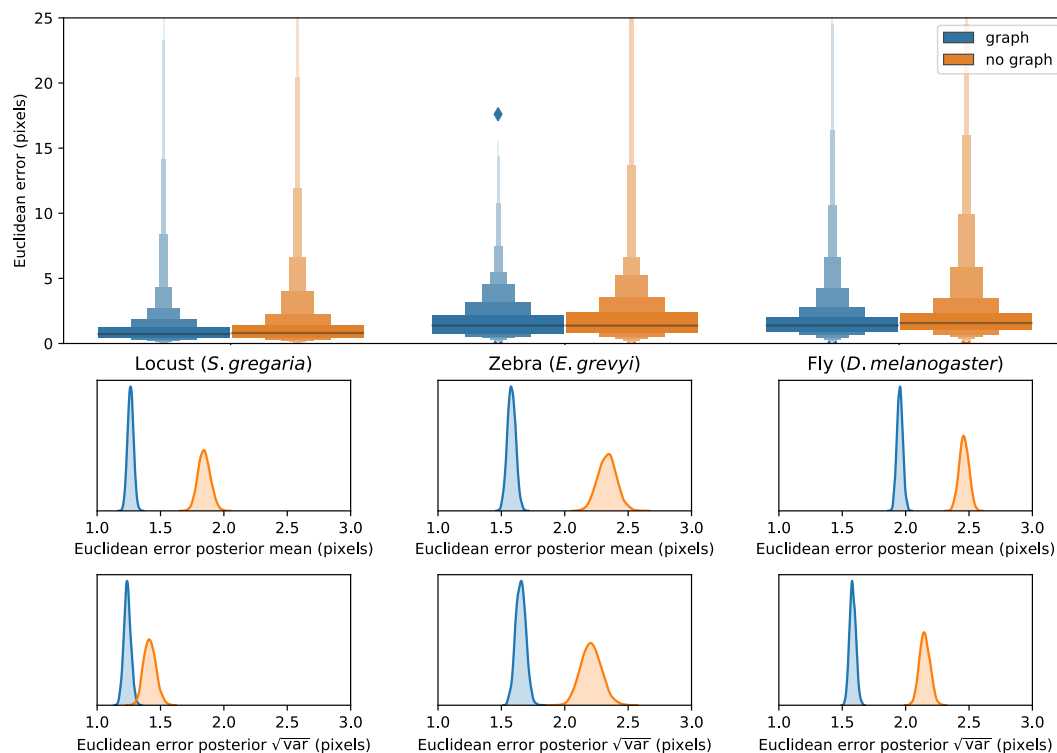
888 **Zuffi S**, Kanazawa A, Berger-Wolf T, Black MJ. Three-D Safari: Learning to Estimate Zebra Pose, Shape, and Texture from Images
889 "In the Wild". In: *International Conference on Computer Vision*; 2019. .

890 **Zuffi S**, Kanazawa A, Jacobs DW, Black MJ. 3D menagerie: Modeling the 3D shape and pose of animals. In: *Proceedings of the*
891 *IEEE Conference on Computer Vision and Pattern Recognition*; 2017. p. 6365–6373.



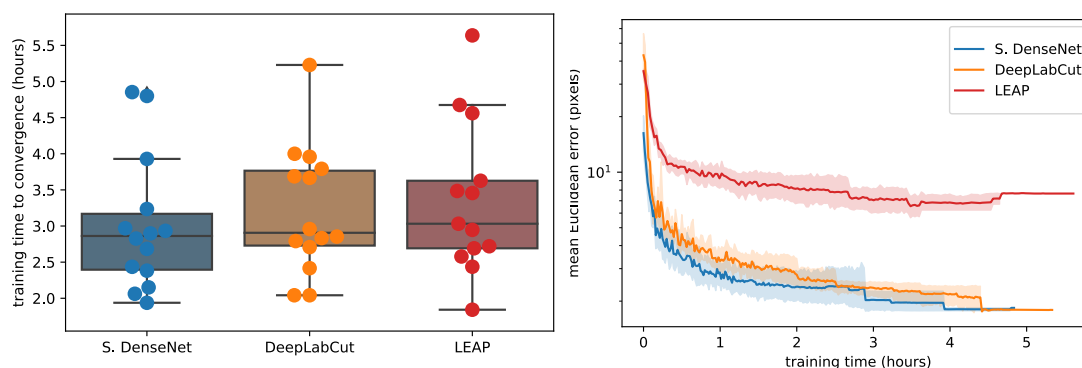
Appendix 1 Figure 1. Our subpixel maxima algorithm increases speed without decreasing accuracy. Prediction accuracy on the fly dataset is maintained across downsampling configurations (**a**). Letter-value plots (**a-top**) show the raw error distributions for each configuration. Visualizations of the credible intervals (99% highest-density region) of the posterior distributions for the mean and variance (**a-bottom**) illustrate statistical differences between the error distributions, where using subpixel maxima decreases both the mean and variance of the error distribution. Inference speed is fast and can be run in real-time on single images (batch size = 1) at ~30-110Hz or offline (batch size = 100) upwards of 1000Hz (**b**). Plots show the inference speeds for our Stacked DenseNet model across downsampling configurations as well as the other models we tested for each of our datasets.

Figure 1-source data 1. Raw prediction errors for experiments in Appendix 1 Figure 1a. See "Methods" for details.



Appendix 1 Figure 2. Predicting the multi-scale geometry of the posture graph reduces error. Letter-value plots (**top**) show the raw error distributions for each experiment. Visualizations of the posterior distributions for the mean and variance (**bottom**) show statistical differences between the error distributions. Predicting the posture graph decreases both the mean and variance of the error distribution.

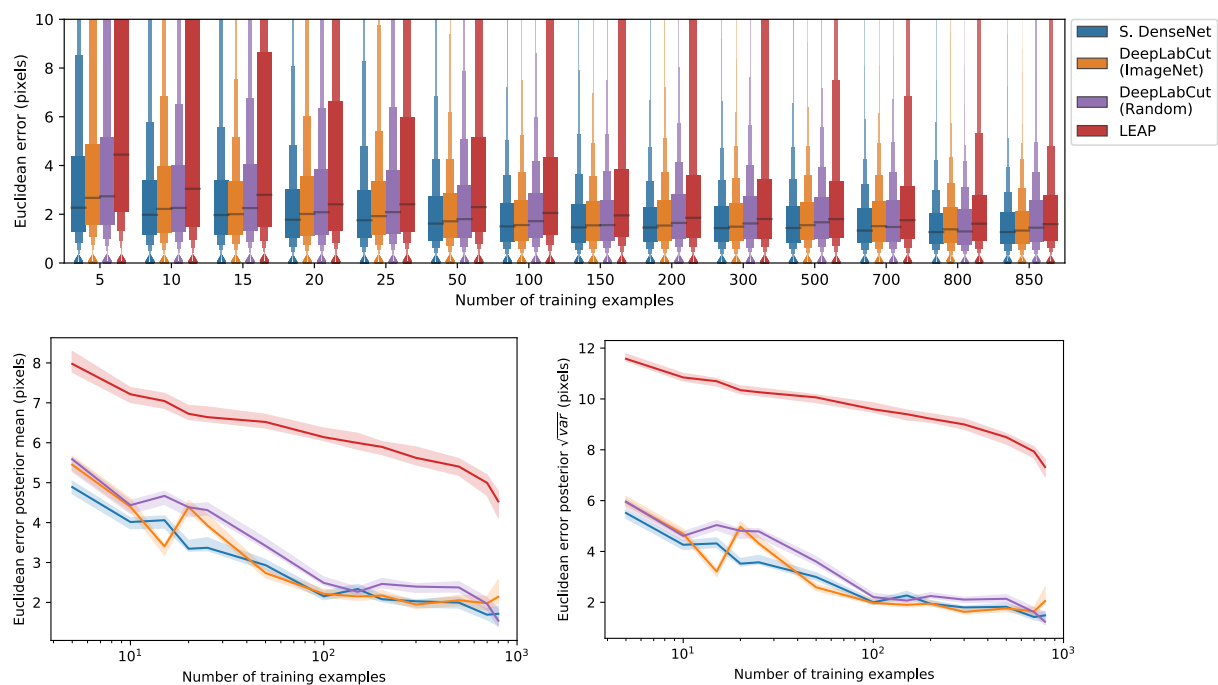
Figure 2-source data 1. Raw prediction errors for experiments in Appendix 1 Figure 2. See "Methods" for details.



Appendix 1 Figure 3. Training time required for our Stacked DenseNet model, the DeepLabCut model (Mathis et al., 2018), and the LEAP model (Pereira et al., 2019) (n=15 per model) using our zebra dataset. Boxplots and swarm plots (**left**) show the total training time to convergence (<0.001 improvement in validation loss for 50 epochs). Line plots (**right**) illustrate the Euclidean error of the validation set during training, where error bars show bootstrapped (n=1000) 99% confidence intervals of the mean. Fully training models to convergence requires only a few hours of optimization (**left**) with reasonable accuracy reached after only 1 hour (**right**) for our Stacked DenseNet model.

Figure 3-source data 1. Total training time for each model in Appendix 1 Figure 3.

Figure 3-source data 2. Mean euclidean error as a function of training time for each model in Appendix 1 Figure 3.



Appendix 1 Figure 4. A comparison of prediction accuracy with different numbers of training examples from our zebra dataset. The error distributions shown as letter-value plots (**top**) illustrate the Euclidean error for the remainder of the dataset not used for training—with a total of 900 labeled examples in the dataset. Line plots (**bottom**) show posterior credible intervals (99% highest-density region) for the mean and variance of the error distributions. We tested our Stacked DenseNet model; the DeepLabCut model (*Mathis et al., 2018*) with transfer learning—i.e., with weights pretrained on ImageNet (*Deng et al., 2009*); the same model without transfer learning—i.e., with randomly-initialized weights; and the LEAP model (*Pereira et al., 2019*). Our Stacked DenseNet model achieves high accuracy using few training examples without the use of transfer learning. Using pretrained weights does slightly decrease overall prediction error for the DeepLabCut model (*Mathis et al., 2018*), but the effect size is relatively small.

Figure 4—source data 1. Raw prediction errors for experiments in Appendix 1 Figure 4. See "Methods" for details.

893 Appendix 2

894 Convolutional neural networks (CNNs)

895 *Artificial neural networks* like CNNs are complex, non-linear regression models that "learn" a hierar-
896 chically-organized set of parameters from real-world data via optimization. These machine learning
897 models are now commonplace in science and industry and have proven to be surprisingly effective for
898 a large number of applications where more conventional statistical models have failed (**LeCun et al.,**
899 **2015**). For computer vision tasks, CNN parameters typically take the form of two-dimensional convo-
900 lutional filters that are optimized to detect spatial features needed to model relationships between
901 high-dimensional image data and some related variable(s) of interest, such as locations in space—e.g.,
902 posture keypoints—or semantic labels (**Long et al., 2015; Badrinarayanan et al., 2015**).

903 Once a training set is generated (Appendix 3), a CNN model must be selected and optimized to
904 perform the prediction task. CNNs are incredibly flexible with regard to how models are specified and
905 trained, which is both an advantage and a disadvantage. This flexibility means models can be adapted
906 to almost any computer vision task, but it also means the number of possible model architectures and
907 optimization schemes is very large. This can make selecting an architecture and specifying hyperpa-
908 rameters a challenging process. However, most research on pose estimation has converged on a set of
909 models that generally work well for this task (Appendix 4).

910 After selecting an architecture, the parameters of the model are set to an initial value and then
911 iteratively updated to minimize some objective function, or *loss function*, that describes the difference
912 between the model's predictive distribution and the true distribution of the data—in other words,
913 the likelihood of the model's output is maximized. These parameter updates are performed using a
914 modified version of the gradient descent algorithm (**Cauchy 1847**) known as *mini-batch stochastic gradient*
915 *descent*—often referred to as simply *stochastic gradient descent* or *SGD* (**Robbins and Monro, 1951; Kiefer**
916 **et al., 1952**). SGD iteratively optimizes the model parameters using small randomly-selected subsamples,
917 or *batches*, of training data. Using SGD allows the model to be trained on extremely large datasets
918 in an iterative "online" fashion without the need to load the entire dataset into memory. The model
919 parameters are updated with each batch by adjusting the parameter values in a direction that minimizes
920 the error—where one round of training on the full dataset is commonly referred to as an *epoch*. The
921 original SGD algorithm requires careful selection and tuning of hyperparameters to successfully optimize
922 a model, but modern versions of the algorithm, such as *ADAM* (**Kingma and Ba, 2014**), automatically
923 tune these hyperparameters, which makes optimization more straightforward.

924 The model parameters are optimized until they reach a convergence criterion, which is some measure
925 of performance that indicates the model has reached a good location in parameter space. The most
926 commonly used convergence criterion is a measure of predictive accuracy—often the loss function
927 used for optimization—on a held-out *validation set*—a subsample of the training data not used for
928 optimization—that evaluates the model's ability to generalize to new "out-of-sample" data. The model is
929 typically evaluated at the end of each training epoch to assess performance on the validation set. Once
930 performance on the validation set stops improving, training is usually stopped to prevent the model
931 from overfitting to the training set—a technique known as *early stopping* (**Prechelt, 1998**).

932 Appendix 3

933 Collecting training data

934 Depending on the variability of the data, CNNs usually require thousands or tens of thousands of
935 manually-annotated examples in order to reach human-level accuracy. However, in laboratory settings,
936 sources of image variation like lighting and spatial scale can be more easily controlled, which minimizes
937 the number of training examples needed to achieve accurate predictions.

938 This need for a large training set can be further reduced in a number of ways. Two commonly used
939 methods include (1) *transfer learning*—using a model with parameters that are pre-trained on a larger
940 set of images, such as the ImageNet database (**Deng et al., 2009**), containing diverse features (**Pratt,**
941 **1993**; **Insafutdinov et al., 2016**; **Mathis et al., 2018**)— and (2) *augmentation*— artificially increasing data
942 variance by applying spatial and noise transformations such as flipping (mirroring), rotating, scaling, and
943 adding different forms of noise or artificial occlusions. Both of these methods act as useful forms of
944 *regularization*—incorporating a prior distribution—that allows the model to generalize well to new data
945 even when the training set is small. Transfer learning incorporates prior information that images from
946 the full dataset should contain statistical features similar to other images of the natural world, while
947 augmentation incorporates prior knowledge that animals are bilaterally symmetric, can vary in their
948 body size, position, and orientation, and that noise and occlusions sometimes occur.

949 **Pereira et al. (2019)** introduced two especially clever solutions for collecting an adequate training
950 set. First, they cluster unannotated images based on pixel variance and uniformly sample images from
951 each cluster, which reduces correlation between training examples and ensures the training data are
952 representative of the entire distribution of possible images. Second, they use *active learning* where
953 a CNN is trained on a small number of annotated examples and is then used to initialize keypoint
954 locations for a larger set of unannotated data. These pre-initialized data are then manually corrected
955 by the annotator, the model is retrained, and the unannotated data are re-initialized. The annotator
956 applies this process iteratively as the training set grows larger until they are providing only minor
957 adjustments to the pre-initialized data. This “human-in-the-loop”-style annotation expedites the process
958 of generating an adequately large training set by reducing the cognitive load on the annotator—where
959 the pose estimation model serves as a “cognitive partner”. Such a strategy also allows the annotator to
960 automatically select new training examples based on the performance of the current iteration—where
961 low-confidence predictions indicate examples that should be annotated for maximum improvement
962 (Figure 1).

963 Of course, annotating image data requires software made for this purpose. **Pereira et al. (2019)**
964 provide a custom annotation GUI written in MATLAB specifically designed for annotating posture using
965 an active learning strategy. **Mathis et al. (2018)** recently added a Python-based GUI in an updated
966 version of their software—including active learning and image sampling methods (see **Nath et al. 2019**).
967 Our framework also includes a Python-based GUI for annotating data with similar features to **Mathis**
968 **et al. (2018)** and **Pereira et al. (2019)**.

969 Appendix 4

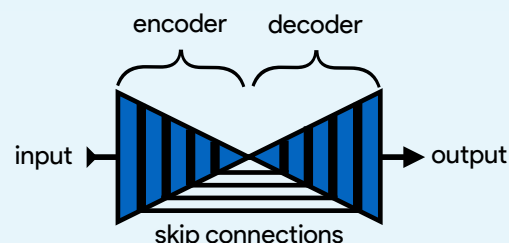
970 Fully-convolutional regression

971 For the task of pose estimation, a CNN is optimized to predict the locations of postural keypoints in an
 972 image. One approach is to use a CNN to directly predict the numerical value of each keypoint coordinate
 973 as an output. However, making predictions in this way removes real-world constraints on the model's
 974 predictive distribution by destroying spatial relationships within images, which negates many of the
 975 advantages of using CNNs in the first place.

976 CNNs are particularly good at transforming one image to produce another related image, or set
 977 of images, while preserving spatial relationships and allowing for translation-invariant predictions—a
 978 configuration known as a *fully-convolutional neural network* or *F-CNN* (Long et al., 2015). Therefore,
 979 instead of directly regressing images to coordinate values, a popular solution (Newell et al., 2016;
 980 Insafutdinov et al., 2016; Mathis et al., 2018; Pereira et al., 2019) is to optimize a F-CNN that transforms
 981 images to predict a stack of output images known as *confidence maps*—one for each keypoint. Each
 982 confidence map in the output volume contains a single, two-dimensional, symmetric Gaussian indicating
 983 the location of each joint, and the scalar value of the peak indicates the confidence score of the
 984 prediction—typically a value between 0 and 1. The confidence maps are then processed to produce the
 985 coordinates of each keypoint.

986 In the case of *multiple pose estimation* where an image contains many individuals, the global geom-
 987 etry of the posture graph is also predicted by training the model to produce *part affinity fields* (Cao
 988 et al., 2017)—directional vector fields drawn between joints in the posture graph—or *pairwise terms*
 989 (Insafutdinov et al., 2016)—vector fields of the conditional distributions between posture keypoints
 990 (e.g., $p(\text{foot}|\text{head})$). This allows multiple posture graphs to be disentangled from the image using graph
 991 partitioning as the vector fields indicate the probability of the connection between joints (see Cao et al.
 992 2017 for details).

Box 1. Encoder-decoder models

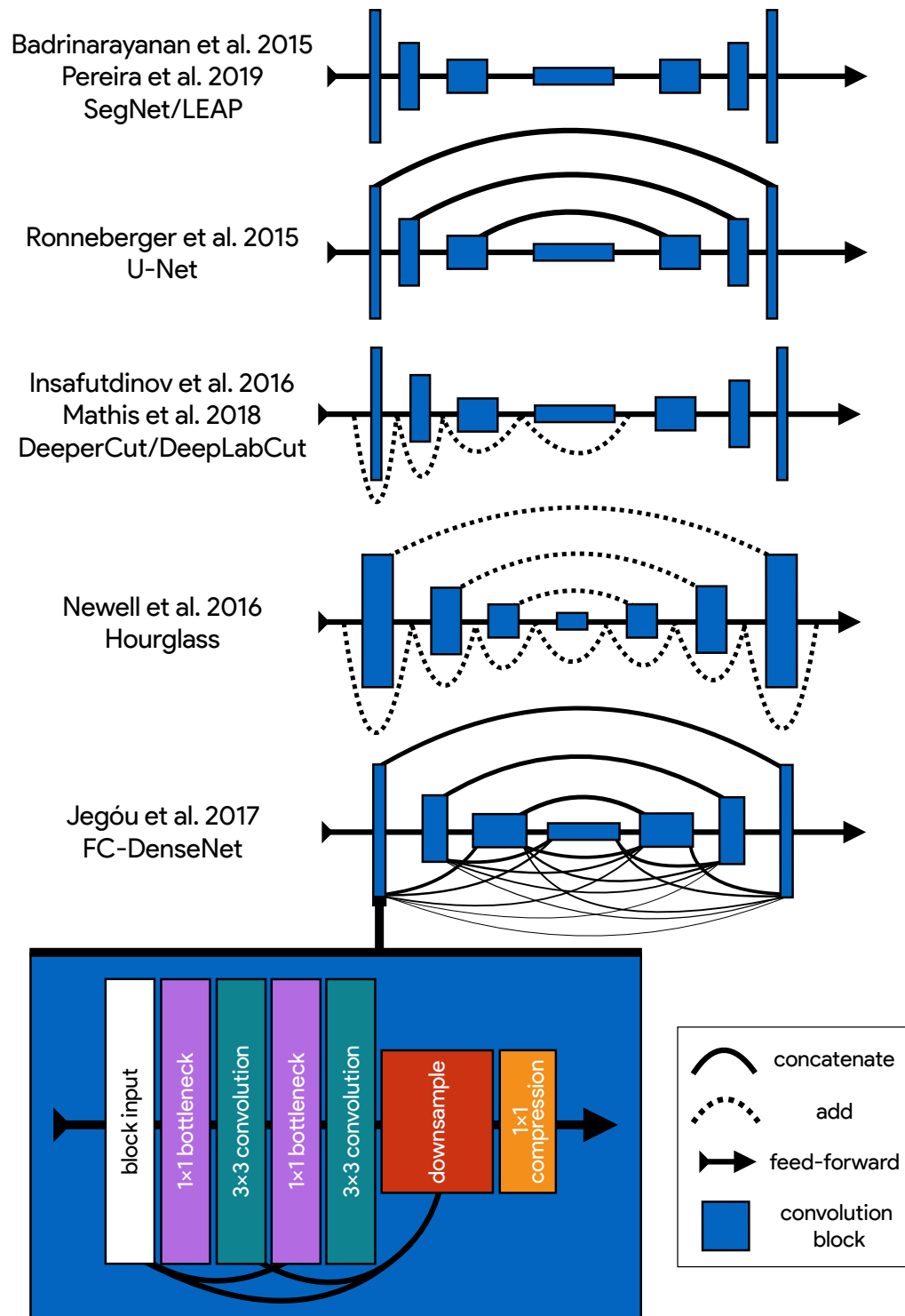


Box 1 Figure 1. An illustration of the basic encoder-decoder design. The encoder converts the input images into spatial features, and the decoder transforms spatial features to the desired output.

A popular type of F-CNN (Appendix 4) for solving posture regression problems is known as an *encoder-decoder* model (Figure 1), which first gained popularity for the task of *semantic segmentation*—a supervised computer vision problem where each pixel in an image is classified into a one of several labeled categories like “dog”, “tree”, or “road” (Long et al., 2015). This model is designed to repeatedly convolve and downsample input images in the bottom-up *encoder* step and then convolve and upsample the encoder’s output in the top-down *decoder* step to produce the final output. Repeatedly applying convolutions and non-linear functions, or *activations*, to the input images transforms pixel values into higher-order spatial features, while downsampling and upsampling respectively increases and decreases the scale and complexity of these features.

Badrinarayanan et al. (2015) were the first to popularize a form of this model —known as *SegNet*— for semantic segmentation. However, this basic design is inherently limited because the decoder relies solely on the downsampled output from the encoder, which restricts the features used for predictions to those with the largest spatial scale and highest complexity. For example, a very deep network might learn a complex spatial pattern for predicting “grass” or “trees”, but because it cannot directly access information from the earliest layers of the network, it cannot use the simplest features that plants are green and brown. Subsequent work by Ronneberger et al. (2015) improved on these problems with the addition of *residual* or *skip connections* between the encoder and decoder, where feature maps from encoder layers are concatenated to those decoder layers with the same spatial scale. This set of connections then allows the optimizer, rather than the user, to select the most relevant spatial scale(s) for making predictions.

Jégou et al. (2017) are the latest to advance the encoder-decoder paradigm. These researchers introduced a fully-convolutional version of Huang et al.’s (2017a) *DenseNet* architecture known as a *fully-convolutional DenseNet*, or *FC-DenseNet*. FC-DenseNet’s key improvement is an elaborate set of feed-forward residual connections where the input to each convolutional layer is a concatenated stack of feature maps from all previous layers. This densely-connected design was motivated by the insight that many state-of-the-art models learn a large proportion of redundant features. Most CNNs are not designed so that the final output layers can access all feature maps in the network simultaneously, and this limitation causes these networks to “forget” and “relearn” important features as the input images are transformed to produce the output. In the case of the incredibly popular ResNet-101 (He et al., 2016) nearly 40% of the features can be classified as redundant (Ayinde and Zurada, 2018). A densely-connected architecture has the advantages of reduced feature redundancy, increased feature reuse, enhanced feature propagation from early layers to later layers, and subsequently, a substantial reduction in the number of parameters needed to achieve state-of-the-art results (Huang et al., 2017a). Recent work has also shown that DenseNet’s elaborate residual connections have the pleasant side-effect of convexifying the loss landscape during optimization (Li et al., 2018), which allows for faster optimization and increases the likelihood of reaching a good optimum.



Appendix 4 Figure 1. An illustration showing the progression of encoder-decoder architectures from the literature—ordered by performance from top to bottom (see Appendix 4 Box 1 for further details). Most advances in performance have come from adding connections between layers in the network, culminating in FC-DenseNet from Jégou et al. (2017). Lines in each illustration indicate connections between convolutional blocks with the thickness of the line indicating the magnitude of information flow between layers in the network. The size of each convolution block indicates the relative number of feature maps (width) and spatial scale (height). The callout for FC-DenseNet (Jégou et al. 2017; bottom-left) shows the elaborate set of skip connections within each densely-connected convolutional block as well as its additions of bottleneck and compression layers (described by Huang et al. 2017a) to increase efficiency (Appendix 8)

1033 Appendix 5

1034 The state of the art for individual pose estimation

1035 Many of the current state-of-the-art models for individual posture estimation are based on the design
 1036 from *Newell et al. (2016)* (e.g., *Ke et al. 2018*, *Chen et al. 2017*; also see benchmark results from *An-*
 1037 *driluka et al. 2014*), but employ various modifications that increase complexity to improve performance.
 1038 *Newell et al. (2016)* employ what they call a *Stacked Hourglass* network (Appendix 4 Figure 1), which con-
 1039 sists of a series of multi-scale encoder-decoder *hourglass* modules connected together in a feed-forward
 1040 configuration (Figure 2). The main novelties these researchers introduce include (1) stacking multiple
 1041 hourglass networks together for repeated top-down-bottom-up inference, (2) using convolutional blocks
 1042 based on the ResNet architecture (*He et al., 2016*) with residual connections between the input and
 1043 output of each block, and (3) using residual connections between the encoder and decoder (similar to
 1044 *Ronneberger et al. 2015*) with residual blocks in between. *Newell et al. (2016)* also apply a technique
 1045 known as *intermediate supervision* (Figure 2) where the loss function used for model training is applied to
 1046 the output of each hourglass as a way of improving optimization across the model's many layers. Recent
 1047 work by *Jégou et al. (2017)* has further improved on this encoder-decoder design (see Appendix 4 Box 1
 1048 and Appendix 4 Figure 1), but to the best of our knowledge, the model introduced by *Jégou et al. (2017)*
 1049 has not been previously applied to pose estimation.

1050 Appendix 6

1051 Overparameterization and the limitations of LEAP

1052 Overparameterization is a key limitation for many pose estimation methods, and addressing this
 1053 problem is critical for high-performance applications. *Pereira et al. (2019)* approached this problem by
 1054 designing their LEAP model after the model from *Badrinarayanan et al. (2015)*, which is a straightforward
 1055 encoder-decoder design (Appendix 4 Figure 1; Appendix 4 Box 1). They benchmarked their model on
 1056 posture estimation tasks for laboratory animals and compared performance with the more-complex
 1057 Stacked Hourglass model from *Newell et al. (2016)*. They found their smaller, simplified model achieved
 1058 equal or better median accuracy with dramatic improvements in inference speed up to 185 Hz. However,
 1059 *Pereira et al. (2019)* first rotationally and translationally aligned each image to improve performance,
 1060 and their reported inference speeds do not include this computationally expensive preprocessing step.
 1061 Additionally, rotationally and translationally aligning images is not always possible when the background
 1062 is complex or highly-variable—such as in field settings—or the study animal has a non-rigid body. This
 1063 limitation makes the LEAP model (*Pereira et al., 2019*) unsuitable in many cases. While their approach is
 1064 simple and effective for a multitude of experimental setups, the LEAP model (*Pereira et al., 2019*) is also
 1065 implicitly limited in the same ways as *Badrinarayanan et al.*'s SegNet model (see Appendix 4 Box 1 for
 1066 details). The LEAP model cannot make predictions using multiple spatial scales and is not robust to data
 1067 variance such as rotations (*Pereira et al., 2019*).

1068 Appendix 7

1069 Linear model fitting with Stan

1070 We estimated the joint posterior $p(\theta_\mu, \theta_\phi | X, y)$ for each model using the No-U-Turn Sampler (NUTS;
 1071 **Hoffman and Gelman 2014**), a self-tuning variant of the Hamiltonian Monte Carlo (HMC) algorithm
 1072 (**Duane et al., 1987**), implemented in Stan (**Carpenter et al., 2017**). We drew HMC samples using 4
 1073 independent Markov chains consisting of 1,000 warm-up iterations and 1,000 sampling iterations for
 1074 a total of 4,000 sampling iterations. To speed up sampling, we randomly subsampled 20% of the data
 1075 from each replicate when fitting each linear model, and we fit each model 5 times to ensure the results
 1076 were consistent. All models converged without any signs of pathological behavior. We performed a
 1077 posterior predictive check by visually inspecting predictive samples to assess model fit. For our priors
 1078 we chose relatively uninformative distributions $\theta_\mu \sim \text{Cauchy}(0, 5)$ and $\theta_\phi \sim \text{Cauchy}(0, 10)$, but we found
 1079 that the choice of prior generally did not have an effect on the final result due to the large amount of
 1080 data used to fit each model.

Appendix 8

Stacked DenseNet

Our Stacked DenseNet model consists of an initial 7×7 convolutional layer with stride 2, to efficiently downsample the input resolution—following *Newell et al. (2016)*—followed by a stack of densely-connected hourglass networks with intermediate supervision (Appendix 5) applied at the output of each network. We also include hyperparameters for the bottleneck and compression layers described by *Huang et al. (2017a)* to make the model as efficient as possible. These consist of applying a 1×1 convolution to inexpensively compress the number of feature maps before each 3×3 convolution as well as when downsampling and upsampling (see *Huang et al. 2017a* and Appendix 4 Figure 1 for details).

Model hyperparameters

For our Stacked Hourglass model we used a block size of 64 filters (64 filters per 3×3 convolution) with a bottleneck factor of 2 ($64/2 = 32$ filters per 1×1 bottleneck block). For our Stacked DenseNet model we used a growth rate of 48 (48 filters per 3×3 convolution), a bottleneck factor of 1 ($1 \times \text{growth rate} = 48$ filters per 1×1 bottleneck block), and a compression factor of 0.5 (feature maps compressed with 1×1 convolution to $0.5m$ when upsampling and downsampling, where m is the number of feature maps). For our Stacked DenseNet model we also replaced the typical configuration of batch normalization and ReLU activations (*Goodfellow et al., 2016*) with the more recently-developed self-normalizing SELU activation function (*Klambauer et al., 2017*), as we found this modification increased inference speed. For the LEAP model (*Pereira et al., 2019*) we used a 1× resolution output with integer-based global maxima because we wanted to compare our more complex models with this model in the original configuration described by *Pereira et al. (2019)*. The LEAP model could be modified to output smaller confidence maps and increase inference speed, but because there is no obvious "best" way to alter the model to achieve this, we forgo any modification. Additionally, applying our subpixel maxima algorithm at high resolution reduces inference speed compared to integer-based maxima, so this would bias our speed comparisons.

Our implementation of the DeepLabCut model

Because the DeepLabCut model from *Mathis et al. (2018)* was not implemented in Keras (a requirement for our pose estimation framework), we re-implemented it. Implementing this model directly in our framework is important to ensure model training and data augmentation are identical when making comparisons between models. As a consequence, our version of this model does not exactly match the description in the paper but is identical except for the output. Rather than using the location refinement maps described by *Insafutdinov et al. (2016)* and post-processing confidence maps on the CPU, our version of the DeepLabCut model (*Mathis et al., 2018*) has an additional transposed convolutional layer to upsample the output to $\frac{1}{4} \times$ resolution and uses our subpixel maxima algorithm.

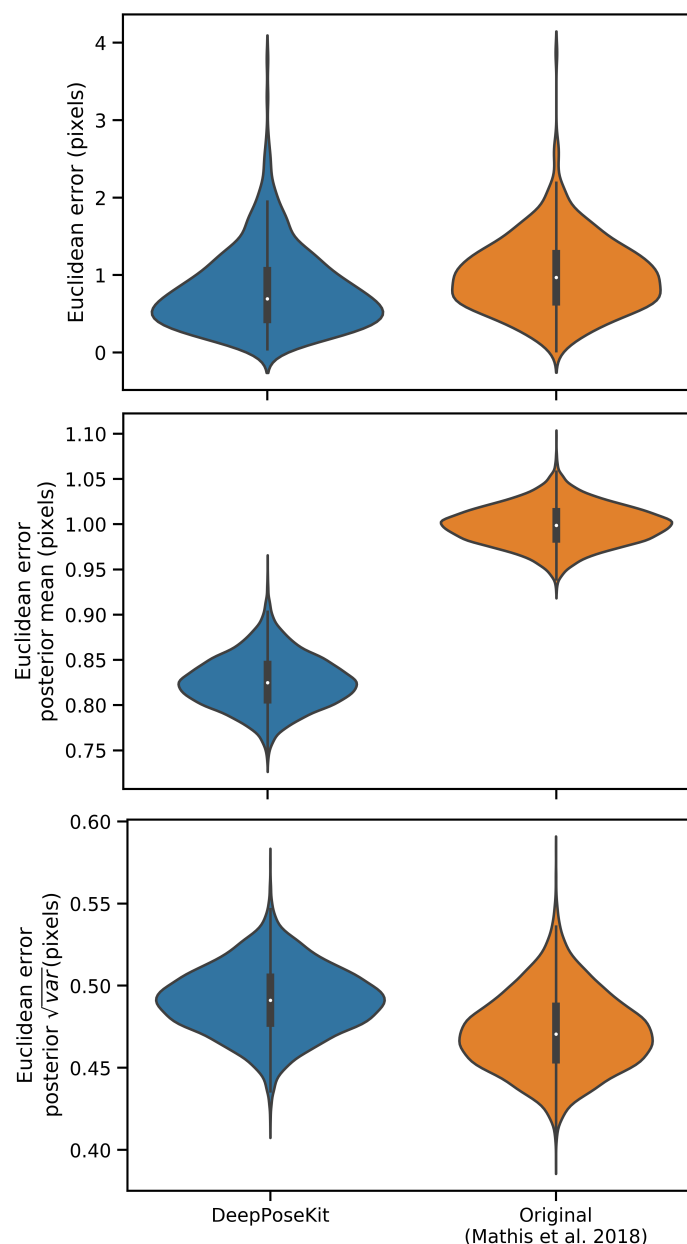
To demonstrate that our implementation of the DeepLabCut model matches the performance described by *Mathis et al. (2018)*, we compared prediction accuracy between the two frameworks using the odor-trail mouse dataset provided by *Mathis et al. (2018)* (downloaded from <https://github.com/AlexEMG/DeepLabCut/>). This dataset consists of 116 images of a freely-moving individual mouse labeled with four keypoints describing the location of the snout, ears, and the base of the tail. See *Mathis et al. (2018)* for further details on this dataset. We trained both models using 95% training and 5% validation data and applied data augmentations for both frameworks using the data augmentation procedure described by *Nath et al. (2019)*. We tried to match these data augmentations as best as possible in DeepPoseKit; however, rather than cropping images as described by *Nath et al. (2019)*, we randomly translated the images independently along the horizontal and vertical axis by drawing from a uniform distribution in the range [-100%, +100%]—where percentages are relative to the size of each axis. Translating the images in this way should serve the same purpose as cropping them.

We trained the original DeepLabCut model (*Mathis et al., 2018*) using the default settings and recommendations from *Nath et al. (2019)* for 1 million training iterations. See *Mathis et al. (2018)*; *Nath et al. (2019)* for further details on the data augmentation and training routine for the original implementation of the DeepLabCut model (*Mathis et al., 2018*). For our re-implementation of the DeepLabCut model (*Mathis et al., 2018*) we trained the model with the same batch size and optimization scheme described in the "Model training" section. We then calculated the the prediction accuracy on the

1130
1131
1132
1133
1134
1135
1136
1137
1138
1139
1140
1141
1142
1143
1144
1145
1146
1147
1148
1149
1150
1151

full data set. We repeated this procedure five times for each model and fit a Bayesian linear model to a randomly selected subset of the evaluation data to compare the results statistically (see Appendix 7).

These results demonstrate that our re-implementation of and modification to the DeepLabCut model (*Mathis et al., 2018*) have little effect on prediction accuracy (Appendix 8 Figure 1). We also provide qualitative comparisons of these results in Appendix 8 Figure 1-Figure supplement 1 and Appendix 8 Figure 1-video 1. For these qualitative comparisons, we also added an additional rotational augmentation (drawing from a uniform distribution in the range [-180°, +180°]) when training our implementation of the DeepLabCut model (*Mathis et al., 2018*) as we noticed this improved generalization to the video for situations where the mouse rotated its body axis. To the best of our knowledge, rotational augmentations are not currently available when using the software from *Mathis et al. (2018)*; *Nath et al. (2019)*, which demonstrates the flexibility of the data augmentation pipeline (*Jung, 2018*) for DeepPoseKit. The inference speed for the odor-trail mouse dataset using our implementation of the DeepLabCut model (*Mathis et al., 2018*) is ~49Hz with a batch size of 64 (offline speeds) and ~35Hz with a batch size of 1 (real-time speeds) at full resolution 640×480, which matches well with results from *Mathis and Warren (2018)* of ~47Hz and ~32Hz respectively. This suggests our modifications did not affect the speed of the model and that our speed comparisons are also reasonable. Because the training routine could be changed for any underlying model—including the new models we present in this paper—this factor is not relevant when making comparisons as long as training is identical for all models being compared, which we ensure when performing our comparisons.



Appendix 8 Figure 1. Prediction errors for the odor-trail mouse dataset from *Mathis et al. (2018)* using the original implementation of the DeepLabCut model (*Mathis et al., 2018; Nath et al., 2019*) and our modified version of this model implemented in DeepPoseKit. Mean prediction error is slightly lower for the DeepPoseKit implementation, but there is no discernible difference in variance. These results indicate that the models achieve nearly identical prediction accuracy despite modification. We also provide qualitative comparisons of these results in Appendix 8 Figure 1-Figure supplements 1 and 2, and Appendix 8 Figure 1-video 1.

Figure 1-Figure supplement 1. Plots of the predicted output for Appendix 8 Figure 1-video 1 comparing our implementation of the DeepLabCut model (*Mathis et al., 2018*) in DeepPoseKit vs. the original implementation from *Mathis et al. (2018); Nath et al. (2019)*. Note the many fast jumps in position for the original version from *Mathis et al. (2018)*, which indicates prediction errors.

Figure 1-Figure supplement 2. Plots of the temporal derivatives of the predicted output for Appendix 8 Figure 1-video 1 comparing our implementation of the DeepLabCut model (*Mathis et al., 2018*) in DeepPoseKit vs. the original implementation from *Mathis et al. (2018); Nath et al. (2019)*. Note the many fast jumps in position for the original version from *Mathis et al. (2018)*, which indicates prediction errors.

Figure 1-video 1. A video comparison of the tracking output of our implementation of the DeepLabCut model (*Mathis et al., 2018*) in DeepPoseKit vs. the original implementation from *Mathis et al. (2018); Nath et al. (2019)*. <https://youtu.be/YFmO5C0hUw4>

Figure 1-source data 1. Raw prediction errors for our DeepLabCut model (*Mathis et al., 2018*) reimplemented in DeepPoseKit in Appendix 8 Figure 1. See "Methods" for details.

Figure 1-source data 2. Raw prediction errors for the original DeepLabCut model from *Mathis et al. (2018)* in Appendix 8 Figure 1. See "Methods" for details.

1152 Appendix 9

1153 Depthwise-separable convolutions for memory-limited applications

1154 In an effort to maximize model efficiency, we also experimented with replacing 3×3 convolutions in
 1155 our model implementations with 3×3 depthwise-separable convolutions —first introduced by *Chollet*
 1156 (*2017*) and now commonly used in fast, efficient “mobile” CNNs (e.g., *Sandler et al. 2018*). In theory this
 1157 modification should both reduce the memory footprint of the model and increase inference speed.
 1158 However we found that, while this does drastically decrease the memory footprint of our already
 1159 memory-efficient models, it slightly decreases accuracy and does not improve inference speed, so we
 1160 opt for a full 3×3 convolution instead. We suspect that this discrepancy between theory and application is
 1161 due to inefficient implementations of depthwise-separable convolutions in many popular deep learning
 1162 frameworks, which will hopefully improve in the near future. At the moment we include this option as
 1163 a hyperparameter for our Stacked DenseNet model, but we recommend using depthwise-separable
 1164 convolutions only for applications that require a small memory footprint such as training on a lower-end
 1165 GPU with limited memory or running inference on a mobile device.

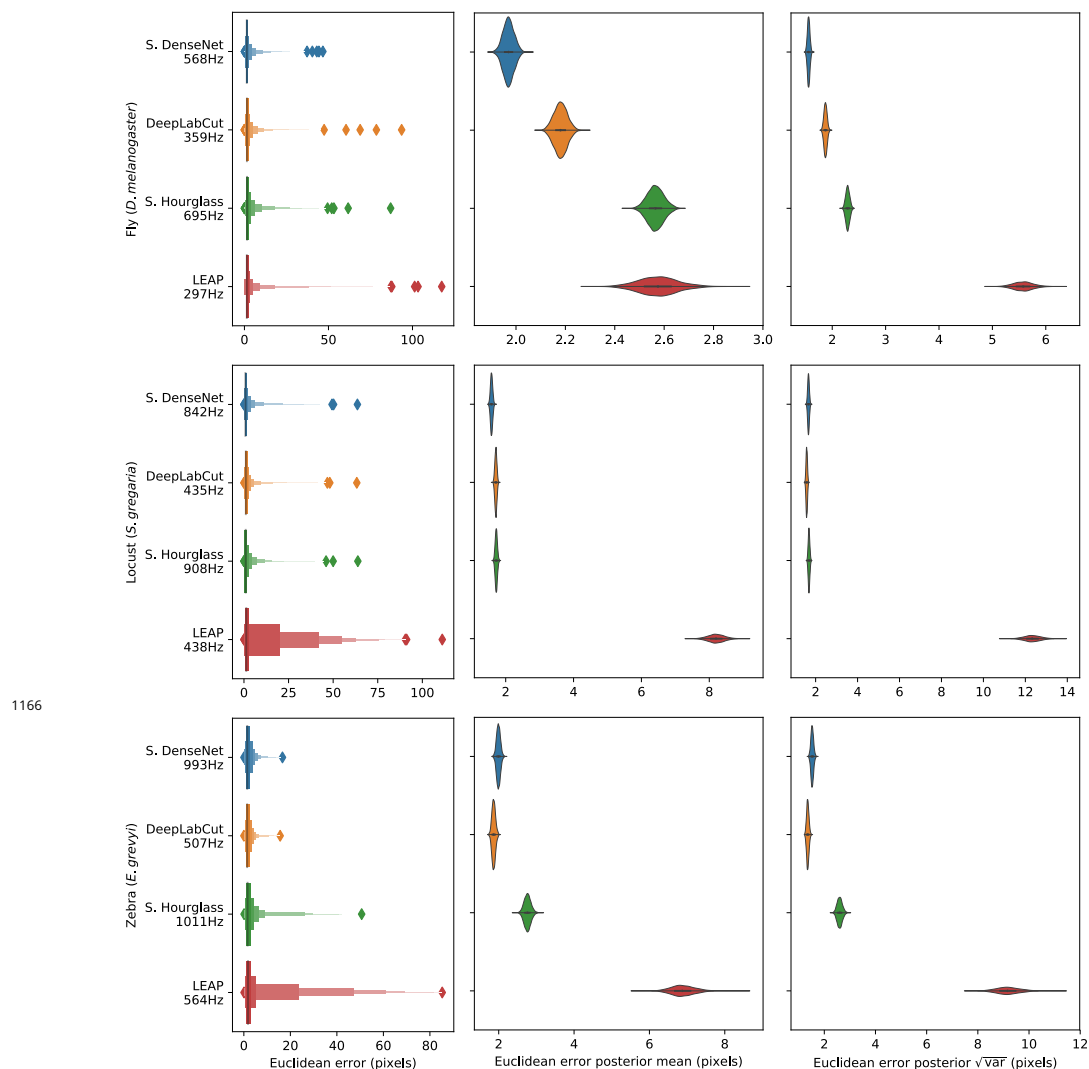


Figure 3-Figure supplement 1. Euclidean error distributions for each model across our three datasets. Letter-value plots (**left**) show the raw error distributions for each model. Violinplots of the posterior distributions for the mean and variance (**right**) show statistical differences between the error distributions. Overall the LEAP model (*Pereira et al., 2019*) was the worst performer on every dataset in terms of both mean and variance. Our Stacked Densenet model was the best performer for the fly dataset, while our Stacked DenseNet model and the DeepLabCut model (*Mathis et al., 2018*) both performed equally well on the locust and zebra datasets. The posteriors for the DeepLabCut model (*Mathis et al., 2018*) and our Stacked DenseNet model are highly overlapping for these datasets, which suggests they are not statistically discernible from one another. Our Stacked Hourglass model (*Newell et al., 2016*) performed equally to the DeepLabCut model (*Mathis et al., 2018*) and our Stacked DenseNet model for the locust dataset but performed slightly worse for the fly and zebra datasets.

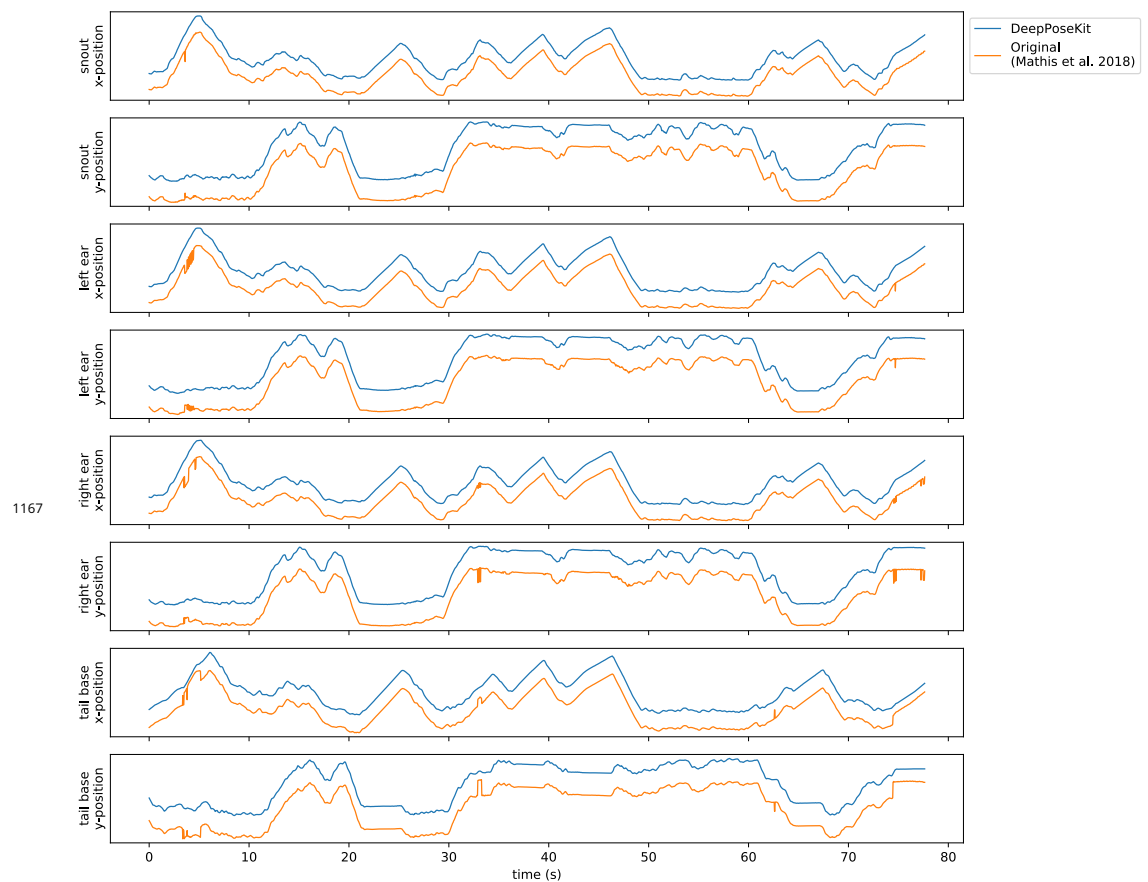


Figure 1-Figure supplement 1. Plots of the predicted output for Appendix 8 Figure 1-video 1 comparing our implementation of the DeepLabCut model (*Mathis et al., 2018*) in DeepPoseKit vs. the original implementation from *Mathis et al. (2018)*; *Nath et al. (2019)*. Note the many fast jumps in position for the original version from *Mathis et al. (2018)*, which indicates prediction errors.

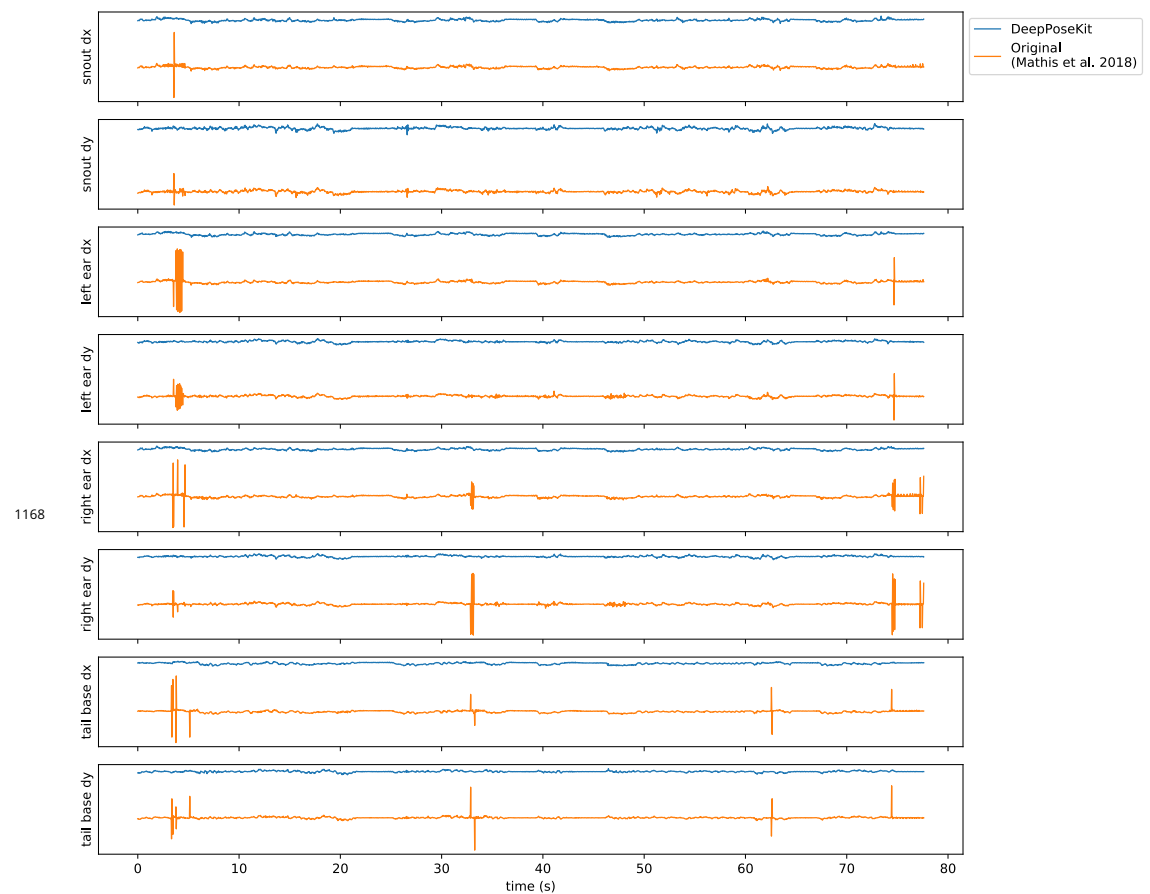


Figure 1-Figure supplement 2. Plots of the temporal derivatives of the predicted output for Appendix 8 Figure 1-video 1 comparing our implementation of the DeepLabCut model (*Mathis et al., 2018*) in DeepPoseKit vs. the original implementation from *Mathis et al. (2018)*; *Nath et al. (2019)*. Note the many fast jumps in position for the original version from *Mathis et al. (2018)*, which indicates prediction errors.